

Quantitative fluorescence analysis reveals dendrite-specific thalamocortical plasticity in L5 pyramidal neurons during learning

Ajit Ray, Joseph A. Christian, Matthew B. Mosso, Eunsol Park, Waja Wegner, Katrin Willig, Alison L. Barth




Angaben zur Veröffentlichung / Publication details:

Ray, Ajit, Joseph A. Christian, Matthew B. Mosso, Eunsol Park, Waja Wegner, Katrin Willig, and Alison L. Barth. 2023. "Quantitative fluorescence analysis reveals dendrite-specific thalamocortical plasticity in L5 pyramidal neurons during learning." *The Journal of Neuroscience* 43 (4): 584–600. <https://doi.org/10.1523/jneurosci.1372-22.2022>.

Nutzungsbedingungen / Terms of use:

CC BY 4.0

Quantitative Fluorescence Analysis Reveals Dendrite-Specific Thalamocortical Plasticity in L5 Pyramidal Neurons during Learning

 Ajit Ray,¹ Joseph A. Christian,¹ Matthew B. Mosso,¹ Eunsol Park,¹ Waja Wegner,^{2,3}  Katrin I. Willig,^{2,3} and  Alison L. Barth¹

¹Department of Biological Sciences, Carnegie Mellon University, Pittsburgh Pennsylvania 15213, ²Optical Nanoscopy in Neuroscience, Center for Nanoscale Microscopy and Molecular Physiology of the Brain, University Medical Center Göttingen, 37099 Göttingen, Germany, and ³Max Planck Institute for Multidisciplinary Sciences, 37077 Göttingen, Germany

High-throughput anatomic data can stimulate and constrain new hypotheses about how neural circuits change in response to experience. Here, we use fluorescence-based reagents for presynaptic and postsynaptic labeling to monitor changes in thalamocortical synapses onto different compartments of layer 5 (L5) pyramidal (Pyr) neurons in somatosensory (barrel) cortex from mixed-sex mice during whisker-dependent learning (Audette et al., 2019). Using axonal fills and molecular-genetic tags for synapse identification in fixed tissue from Rbp4-Cre transgenic mice, we found that thalamocortical synapses from the higher-order posterior medial thalamic nucleus showed rapid morphologic changes in both presynaptic and postsynaptic structures at the earliest stages of sensory association training. Detected increases in thalamocortical synaptic size were compartment specific, occurring selectively in the proximal dendrites onto L5 Pyr and not at inputs onto their apical tufts in L1. Both axonal and dendritic changes were transient, normalizing back to baseline as animals became expert in the task. Anatomical measurements were corroborated by electrophysiological recordings at different stages of training. Thus, fluorescence-based analysis of input- and target-specific synapses can reveal compartment-specific changes in synapse properties during learning.

Key words: apical dendrite; intrabodies; learning; LTP; plasticity; POm thalamus

Significance Statement

Synaptic changes underlie the cellular basis of learning, experience, and neurologic diseases. Neuroanatomical methods to assess synaptic plasticity can provide critical spatial information necessary for building models of neuronal computations during learning and experience but are technically and fiscally intensive. Here, we describe a confocal fluorescence microscopy-based analytical method to assess input, cell type, and dendritic location-specific synaptic plasticity in a sensory learning assay. Our method not only confirms prior electrophysiological measurements but allows us to predict functional strength of synapses in a pathway-specific manner. Our findings also indicate that changes in primary sensory cortices are transient, occurring during early learning. Fluorescence-based synapse identification can be an efficient and easily adopted approach to study synaptic changes in a variety of experimental paradigms.

Received July 7, 2022; revised Oct. 28, 2022; accepted Nov. 23, 2022.

Author contributions: A.R. and A.L.B. designed research; A.R., J.A.C., and E.P. performed research; W.W. and K.I.W. contributed unpublished reagents/analytic tools; A.R., J.A.C., and M.B.M. analyzed data; A.R. and A.L.B. wrote the paper.

This work was supported by the Carnegie Mellon Neuroscience Institute–Indian Institute of Science Fellowship Program (A.R.), National Institutes of Health Grants R21 MH123906 and R01 MH114103 (A.L.B.), and the Max Planck Institute for Multidisciplinary Sciences (K.I.W.). We thank Joanne Steinmiller for animal care and Rachel Swindell for technical assistance.

The authors declare no competing financial interests.

Correspondence should be addressed to Alison L. Barth at albarth@andrew.cmu.edu.

<https://doi.org/10.1523/JNEUROSCI.1372-22.2022>

Copyright © 2023 the authors

Introduction

Synaptic plasticity underlies the remarkable ability of the brain to respond and reorganize in response to experience. Learning-associated changes, particularly at excitatory synapses, occur across the cerebral cortex under a variety of experimental conditions (Riout-Pedotti et al., 2000; Yang et al., 2009; Biane et al., 2016; Audette et al., 2019), but analyses have typically focused on either presynaptic or postsynaptic elements. Thus, the identity of the neural circuits that are altered during learning remains poorly defined, and the connection between anatomic changes and functional output is unclear. Input- and target-specific anatomic studies can provide essential information to constrain

models for synaptic plasticity during learning and link cellular events to network plasticity but have not been well explored in learning paradigms.

Higher-order thalamocortical pathways show marked changes in functional properties during learning and recovery from injury (Tennant et al., 2017; Pardi et al., 2020), and these changes are rapidly initiated at the onset of training in a sensory association task (Audette et al., 2019). We took advantage of these well-documented changes to develop quantitative, fluorescence-based anatomical methods for detection of structural correlates of plasticity during learning. Fluorescence-based synapse analysis leverages the extended color palette of fluorescent proteins as well as the broad availability of confocal microscopy for analysis, and molecular genetic reagents can selectively label targeted cell types, critical for defining circuit-specific changes (Gross et al., 2013; Fortin et al., 2014; Kuljis et al., 2019, 2021; Bensussen et al., 2020; Graves et al., 2021). In addition, compared with electron microscopy (EM; Bock et al., 2011; Kasthuri et al., 2015; Rodriguez-Moreno et al., 2018), fluorescence-based analyses are amenable to rapid analysis of large numbers of subjects, critical for studies where there is substantial variability in synapse density (Chandrasekaran et al., 2015) or behavior (Bernhard et al., 2020; Gilad and Helmchen, 2020).

We selectively expressed a postsynaptic density protein 95 (PSD95)-labeling, mCitrine-coupled FingR intrabody (Gross et al., 2013; Wegner et al., 2022) in layer 5 (L5) Rbp4-Cre pyramidal (Pyr) neurons in conjunction with a tdTomato fluorophore in axons from the higher-order posterior medial (POM) nucleus of the thalamus to identify thalamocortical synapses. Because the PSD in EM is highly correlated with synaptic strength (Cheetham et al., 2014), and PSD95 increases with synaptic potentiation *in vitro* (Ehrlich and Malinow, 2004; Meyer et al., 2014; Hruska et al., 2018), this marker can serve as a proxy for synaptic strength. Genetically targeted and fluorescently labeled PSD95 has been used to monitor synaptic dynamics (Gray et al., 2006; Cane et al., 2014; Fortin et al., 2014; Subramanian et al., 2019) and has the added advantage of enabling quantitative analysis of synaptic morphology in different dendritic compartments within the same neuron. Importantly, PSD95 labeling using FingR reagents does not alter synaptic function compared with overexpression of fluorescently tagged PSD95 (Gross et al., 2013).

Using digital analysis of confocal images from fixed tissue, presynaptic and postsynaptic elements were detected and aligned to identify putative synaptic contacts and monitor morphologic changes across the learning trajectory. Whole-cell patch-clamp recordings indicate that POM inputs onto L5 Pyr neurons are potentiated at the onset of sensory association training (Audette et al., 2019). Thus, we predicted that POM-assigned PSD95 puncta would increase in size in L5 and also L1, where *in vivo* imaging studies have identified changes in dendritic spines and axonal activity during learning (Kuhlman et al., 2014; Lai et al., 2018; Pardi et al., 2020).

Analysis of synapses within L5a indicate that POM-assigned PSD95-FingR-labeled synapses onto Pyr neurons rapidly increase in size during the first day of training in a sensory association task. This postsynaptic increase is accompanied by a marked change in the size of POM axonal boutons within L5a, indicating coordination of presynaptic and postsynaptic changes at the onset of learning. However, despite evidence that distal dendrites of Pyr neurons within L1 can display anatomic plasticity in response to experience (Yang et al., 2009; Fu et al., 2012; Kuhlman et al., 2014; Chen et al., 2015; Lai et al., 2018), we found that this plasticity was not detected at POM

thalamic inputs. At the same time that thalamocortical synapses within L5a were increasing in size, our analysis indicated that thalamocortical synapses in L1 reduced in size. Anatomical changes were short-lived, renormalizing to baseline levels after several days of training. These data indicate that fluorescence-based analyses of input- and target-specific synapses are feasible and provide new insights into the separate regulation of discrete dendritic compartments during sensory learning.

Materials and Methods

Reagents. All chemicals were purchased from Sigma-Aldrich unless otherwise indicated.

Animals. Experimental procedures were conducted in accordance with the National Institutes of Health guidelines and approved by the Institutional Animal Care and Use Committee at Carnegie Mellon University. Both male and female mice were used for all analyses. Rbp4-Cre transgenic mice (heterozygous males and females; stock #031125-UCD, MMRRC; RRID:MMRRC_031125-UCD) were used for PSD95-FingR-Citrine based thalamocortical synapse analysis. A subset of both intertelencephalic and pyramidal tract neurons in L5 are labeled in this strain (Gerfen et al., 2013). For channelrhodopsin (ChR2)-mediated analysis of POM thalamocortical quantal EPSCs (qEPSCs), Rbp4-Cre (both heterozygous and wild-type) and C57BL/6J (strain #000664, The Jackson Laboratory; RRID:IMSR_JAX:000664) mice were used.

Stereotaxic surgeries. Stereotaxic surgeries were performed at postnatal day (P) 15–20, and animals underwent automated sensory association training (SAT) 6–9 d later, followed by perfusion at P 25–30. For PSD95-FingR-Citrine labeling, ~150 nl of a 1:5 mixture of adeno-associated virus (AAV)1-hSyn-DIO-PSD95-FingR-Citrine virus (Gross et al., 2013; Wegner et al., 2022; titer unknown) and AAV1-hSyn-DIO-eCFP virus (4.2×10^{12} GC/ml, Penn Vector core) for postsynaptic labeling was injected into left barrel cortex (from bregma, $x = -3$, $y = -0.9$, $z = -0.5$ mm from pial surface), and 400 nl of AAV2-CAG-tdTomato (2×10^{13} GC/ml; catalog #59462-AAV2, Addgene; RRID:Addgene_59462) into left POM (from bregma, $x = -1.05$, $y = -1.8$, $z = -3.3$ mm from pial surface) in isoflurane-anesthetized Rbp4-Cre mice (Fig. 1). For ChR2-mediated EPSC experiments, 450 nl of AAV1-hSyn-hChR2 (H134R)-eYFP (1.1×10^{13} GC/ml; catalog #26973-AAV1, Addgene; RRID:Addgene_26973) was injected into left POM. Injections were conducted through two separate craniotomies using a Nanoject II (Drummond Scientific) for the cortex, and a Hamilton syringe injector (Stoelting) for the POM, respectively. Animals were provided subcutaneous analgesia (Ketoprofen) postoperatively.

Automated animal training. We used an automated home-cage system for associating whisker stimulation with a water reward to induce sensory learning in mice as described previously (Audette et al., 2019; Bernhard et al., 2020; Lee et al., 2021). After 2 d of acclimation in the modified home-cage setup without any conditioned stimulus, SAT was initiated, where trials were freely initiated by nose pokes at a recessed water port driving an infrared beam break. For 80% of trials, nose pokes triggered trial onset with a random variable delay (0.2–0.8 s) before the delivery of a gentle air-puff stimulus directed against the right facial vibrissae (~6 psi, 0.5 s duration). Note that animals rapidly habituate to this gentle stimulus, where aversive air puffs are typically 5–10× stronger (30–60 psi; Zhang et al., 2018; Lucantonio et al., 2021). A water reward (~6–20 μ l) was delivered at the lick port 0.5 s after stimulus offset, followed by a 1 s time-out. For the remaining 20% of (blank) trials, nose pokes triggered a similar trial structure but without the air puff or the water reward. Trial structure was randomly determined. SAT animals underwent this training for 1–5 d. Age-matched control animals were housed in the training cages without coupled whisker stimulation for 3–7 d. For ChR2 experiments, all mice underwent 2 d of acclimation before 5 d of training or extended acclimation (i.e., control). Behavioral performance was calculated as the difference in anticipatory lick rates (0.7–1 s following trial onset) for stimulus trials versus blank trials ($\text{Lick frequency}_{\text{Stim}} - \text{Lick frequency}_{\text{Blank}}$; $L_{\text{Stim}} - L_{\text{Blank}}$; Audette et al.,

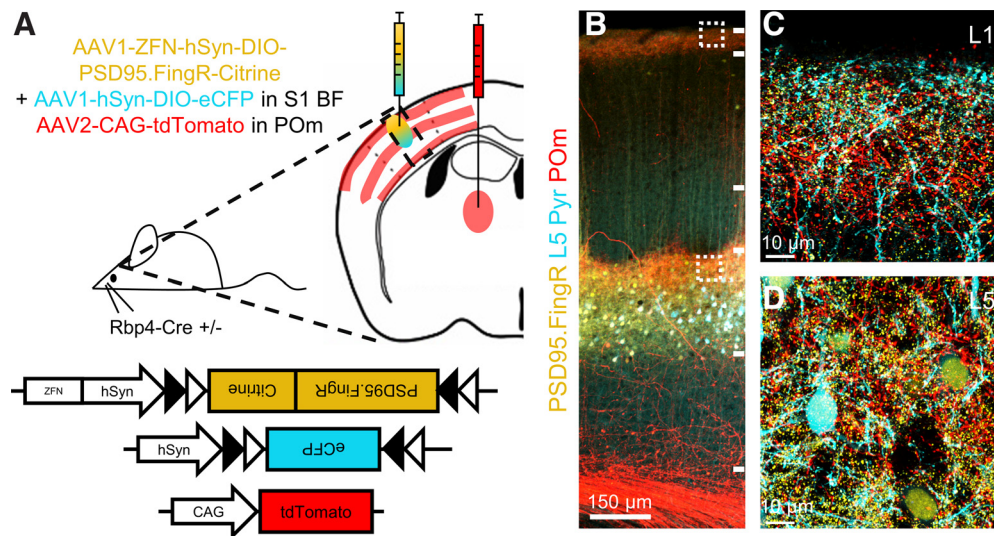


Figure 1. Genetically encoded fluorescent markers for thalamocortical synapse detection. **A**, Top, Schematic demonstrating the stereotaxic delivery of viral constructs into Rbp4-Cre mouse brains. A mixture of Cre-dependent PSD95.FingR-Citrine and eCFP virus was injected into S1 barrel field, allowing for selective labeling of PSD95 postsynaptic sites (yellow) and a cell fill, respectively (cyan), in L5 Pyrs. Thalamocortical axons were labeled in red by a stereotaxic delivery of tdTomato virus into POm. Diagram on right shows characteristic labeling pattern of the viral constructs in S1 barrel cortex and thalamus. Bottom, AAV construct designs. **B–D**, Low-magnification images showing the characteristic expression pattern of the three viruses in S1. High-magnification images from **C** (L1) and **D** (L5) from **B**.

2019). Mean anticipatory lick rates for each animal were calculated in 4 h bins across any given 24 h period (12:00 P.M.–11:59 A.M.) throughout the acclimation and/or SAT periods. Only bins having >10 trials containing both trial types were used for calculations. Performance values were also calculated for the last 20% of trials of any given 24 h period to correlate synaptic measurements with animal behavior.

Tissue processing and histology. At midday following SAT or an extended acclimation period, mice were deeply anesthetized with isoflurane and transcardially perfused using 20 ml $1\times$ PBS, pH 7.4, followed by 20 ml 4% paraformaldehyde in $1\times$ PBS (4% PFA, pH 7.4). Brains were then removed and postfixed overnight at 4°C in 4% PFA before transfer into 30% sucrose in $1\times$ PBS. After osmotic equilibration, ~50- μ m-thick free-floating brain sections were collected in $1\times$ PB using a freezing microtome (Leica Biosystems). Sections where POm axon terminals overlapped with PSD95.FingR-labeled target cells in L5 of barrel cortex were mounted on slides for confocal imaging.

Image acquisition. Sections were imaged using the LSM 880 Axio Observer microscope (Carl Zeiss), using 63 \times oil-immersion objective lens (Plan-Apochromat, NA 1.40, oil) with the pinhole set at 1.0 Airy disk unit for all fluorescence channels. Image size was 1024 \times 1024 pixels, and the zoom factor was set at 0.9 with a 0.3 μ m Z-step size, resulting in voxel dimensions of 0.146 \times 0.146 \times 0.3 μ m (X, Y, and Z). Resultant image stacks were typically 149.5 \times 149.5 \times \leq 35 μ m. Optimal laser intensities and gains for each channel were set to avoid pixel undersaturation or oversaturation for each field of view (FOV) independently. Images were stored in CZI format for subsequent analyses.

For PSD95.FingR analysis, FOVs centered on either L1 or mainly L5a including L4–L5a boundary in the barrel cortex were captured, using the tdTomato-labeled POm axonal fibers as guides. The wavelength settings for the different channels were as follows: CFP (excitation wavelength 405 nm; emission range 435–514 nm), YFP (excitation 514 nm; emission 518–553 nm), and tdTomato (excitation 561 nm; emission 562–620 nm).

Digital reconstruction. All analyses were conducted using Imaris x64 software with the filament tracer plug-in (version 8.4.1; Bitplane). Viral labeling of PSD95.FingR-Citrine was very dense, rendering it difficult to assess the distribution of synapses across individual dendritic arbors. As the DIO-expression system restricted the expression of our postsynaptic labeling constructs to L5 Pyr cells, we chose to perform a limited region-based analysis (puncta from several different L5 Pyr neurons) in FOVs centered on either L1 or L5a using Imaris. We use a representative L5a FOV to demonstrate our reconstruction pipeline (Fig. 2). Regions of

interest (ROIs) containing PSD95.FingR signal were selected from raw confocal image stacks in S1 barrel cortex (Fig. 2A). The images were then gain adjusted to visualize synaptic PSD95.FingR puncta by adjusting background pixels to near black to allow delineation of puncta borders and reduction of pixel noise (Fig. 2B). FingR-Citrine puncta were reconstructed as surface objects using the Imaris 3D watershed algorithm (Surfaces macro; image segmentation) to cover maximal PSD95 punctate signal without capturing background voxels (Fig. 2C). The expected size for objects to be masked was set to 0.4 μ m background-corrected size (without smoothing), based on median PSD size estimated to be between ~0.3 and 0.5 μ m by EM (Sheng and Hoogenraad, 2007) and the average PSD95 puncta measured in our optical sections. The same tool was used to split 3D fused objects (puncta that were close in space and could not be separated) derived from PSD95.FingR punctate signals using seed points (white dots) that mark individual puncta. A quality filter was set to generate a mean object size of 0.4 μ m (Fig. 2D). Objects were filtered at a size \geq 3 voxels (\geq 0.438 μ m if voxels are arranged linearly in x - y) to visualize all PSD95.FingR surface objects (Fig. 2E). As soma were also labeled using Citrine-tagged PSD95.FingR because of the autoregulatory zinc finger motif, we rendered soma using the same Surfaces tool using absolute intensity and contour smoothing with a size of 0.2 μ m (Fig. 2F). PSD95 synaptic puncta were filtered to be at least 0.2 μ m distant from the soma reconstruction (edge to edge; Fig. 2G–I). POm axons were reconstructed from tdTomato-labeled fluorescence signal in the same image ROI (Fig. 2J). Images were gain adjusted as described earlier to maximize signal to noise (Fig. 2K). Following this, boutons were reconstructed using the Surfaces tool with expected background-corrected mask size (without smoothing) set at 0.5 μ m based on earlier EM measurements and average sizes of boutons measured in our optical sections (Fig. 2L; (Rodriguez-Moreno et al., 2020)). The surfaces were then split with a quality filter set at 0.5 μ m and filtered for objects \geq 3 voxels in size (Fig. 2M–O). To compensate for red fluorescence drop off with increasing Z-depth in our image stack, POm bouton reconstructions were adjusted separately for different depths and then combined. Reconstructed PSD95.FingR puncta that were $<$ 0.15 μ m from reconstructed POm boutons (touching, edge-to-edge distance) using the Imaris distance threshold plug-in were identified as POm-assigned PSD95 sites (Fig. 2P–T).

Image analysis. Reconstruction thresholds between FOVs or experimental groups were analyzed in batches and blind to experimental condition. The criteria for inclusion of any set of puncta in our study relied on the fluorescence signal being clearly punctate with an absence of

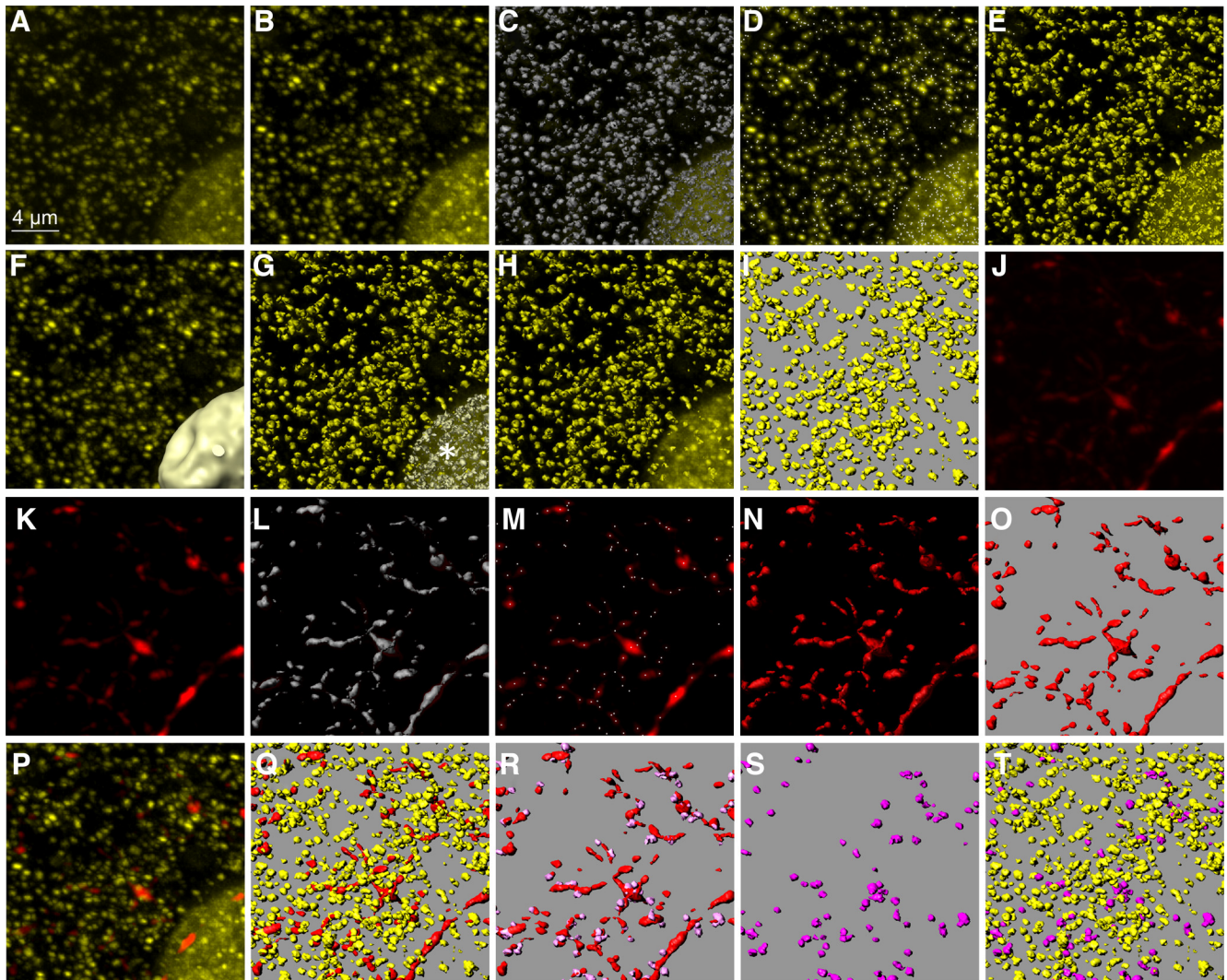


Figure 2. Reconstruction pipeline for presynaptic POM boutons and associated PSD95 puncta. **A**, ROI from raw confocal image stack of PSD95.FingR signal in L5a of S1 barrel cortex. **B**, Gain-adjusted ROI to visualize synaptic PSD95.FingR puncta. **C**, 3D surface masks (gray) constructed in Imaris covering maximal PSD95 punctate signal without capturing background voxels. **D**, PSD95 puncta were split using seed points (white dots) to separate fused 3D masks. **E**, Objects were filtered at a size of ≥ 3 voxels to visualize all PSD95.FingR surface objects (yellow). **F**, 3D surface mask of somatic PSD95.FingR. **G**, PSD95.FingR-puncta are filtered by distance from cell soma objects as in **F**. Light yellow objects (asterisk) are somatic puncta to be excluded. **H**, PSD95.FingR surfaces that exclude puncta inside and on the surface of the labeled soma. **I**, Same as **H** but without the overlaid fluorescence. **J**, Same ROI showing raw confocal image stack of tdTomato-labeled POM presynaptic axons. **K**, Gain-adjusted ROI to visualize tdTomato-labeled POM boutons. **L**, 3D surface masks (gray) constructed in Imaris to cover maximal tdTomato signal without capturing background pixels. **M**, POM boutons were split using seed points (white dots) to separate fused 3D masks. **N**, Finally, POM bouton surface objects were filtered for objects with a size ≥ 3 voxels. **O**, Same as **N** but without the overlaid fluorescence. **P**, Overlaid fluorescent image stacks showing PSD95.FingR and POM boutons from **A** and **J**, respectively. **Q**, Overlaid images of yellow PSD95.FingR surfaces from **I** and red POM boutons from **O**. **R**, PSD95.FingR puncta were filtered to be $< 0.15 \mu\text{m}$ from POM boutons (edge-to-edge distance). PSD95.FingR puncta (light pink) touching red POM boutons. **S**, Isolated POM-assigned PSD95.FingR puncta. **T**, POM-assigned puncta (pink) in a field of unassigned PSD95.FingR puncta (yellow).

oversaturated or undersaturated pixels, properties that can be influenced by viral transduction time, multiplicity of infection, or imaging parameters. Although these criteria can lead to high variability in our dataset, these are sample-identity independent and were not biased toward any particular experimental group (Figs. 3, 4). We plotted image acquisition parameters (laser intensity and camera gain) and Imaris analytical pipeline thresholds (masking/watershedding for object contours from Fig. 2C and quality filter for object splitting from Fig. 2D) for individual animal images and did not observe a significant difference between either the control or trained groups (Fig. 3). Because molecular genetic reagents for synaptic labeling were nonsaturating (Neither all POM axons nor all L5 Pyr neurons were labeled.), the absolute number of boutons and PSD95 puncta detected within a sample could vary widely. However, there was no systematic difference across experimental groups in labeling density (Fig. 4). Overall, the density of labeled PSD95 puncta were \sim threefold higher in L5a than L1, and this did not significantly change with training (Fig. 4B; ratio of L5 to L1 PSD95

densities, control 3.392 ± 0.466 vs SAT 2.706 ± 0.236 ; unpaired $t_{(17)} = 1.07$; $p = 0.30$). These data indicate that despite variability in the absolute number of virally transduced cells across animals, these values were not systematically different between control and trained animals.

Size and intensity measurements of both presynaptic and postsynaptic puncta showed wide variation within and across animals because of varying expression and/or transduction of viral copies and tissue processing and age, and can be dependent on imaging settings.

For higher-fidelity bouton reconstructions, we randomly selected multiple and independent axonal segments (5–12 contiguous-bouton-long stretches with clear outlines) located at different X, Y, and Z positions in individual FOVs. Segments were selected without regard to their association with PSD95.FingR and POM boutons were selected blind to the experimental group, and analyses were repeated by two different observers. We then corrected the selected stretches to remove inter-bouton segments and fix aberrant fragmentation and/or fusion of reconstructed boutons. We noticed substantial variability in the size of

boutons within selected segments, indicating that we were capturing bona fide variation in bouton morphology. After bouton reconstruction, we used an edge-to-edge maximum distance of $<0.15\ \mu\text{m}$ between the 3D renderings of boutons and PSD95 puncta to identify putative POM synapses. This was at the diffraction limit given our imaging parameters, and setting a distance threshold less than this value did not change mean puncta size. Because the true distance between presynaptic and postsynaptic elements across the synaptic cleft is $\sim 0.02\ \mu\text{m}$, these puncta will include some false positives.

As a distance limited within-sample control, unassigned PSD95.FingRs were defined as puncta that were within $0.5\text{--}1\ \mu\text{m}$ distance (edge to edge) from selected axonal boutons, and $>0.15\ \mu\text{m}$ (edge-to-edge) from any other POM axon in the FOV (i.e., all boutons and interbouton segments).

For presynaptic POM boutons, we used volume (μm^3) as an indicator of size. Bouton volume was chosen as we did not have a specific marker for the active zone and to account for the possibility of multiple active zones within multisynaptic boutons. On the other hand, surface area (μm^2) was chosen as an indicator of size for postsynaptic PSD95 signal. Surface area acts as a better measure for PSD95 structures as they are flattened disk-like structures in EM. Volume and surface area measurements from our 3D reconstructed surfaces were well correlated.

Bassoon immunostaining and analysis. Immunohistochemical validation of putative POM synapses on L5 Pyrs was conducted using immunostaining for the presynaptic marker Bassoon for a subset of tissue specimens. Briefly, the sections were blocked (5% donkey serum, 0.5% Triton X-100, and $1\times$ PBS) for 2 h, and then incubated for 40 h at 4°C with mouse anti-Bassoon primary antibody (1:500 in blocking solution; catalog #VAM-PS003, Enzo Life Sciences). Slices were rinsed five times with 0.5% PBST and then incubated with Alexa Fluor 405 anti-mouse secondary antibody (1:500 dilution in $1\times$ PBS; catalog A-31553, Invitrogen). Sections were imaged, and 3D reconstructions of POM boutons and PSD95 puncta were performed to identify POM synapses on L5 Pyr as described above. Within this subset of reconstructed synapses, immunolabeling was manually assessed within individual optical slices to check whether Bassoon was found within the boundaries of the reconstructed POM bouton fluorescence juxtaposed against or overlapping with POM-assigned PSD95 signal. This analysis was restricted to the top $6\ \mu\text{m}$ of the slice because of incomplete penetration of the Bassoon antibody (Kuljis et al., 2019).

Acute brain slice preparation. Brain slices were prepared as described in (Audette et al., 2019). Briefly, isoflurane anesthetized mice were killed by decapitation between 11:00 A.M. and 3:00 P.M. pm. Angled slices $350\ \mu\text{m}$ thick (one cut, 45° rostralateral and 25° rostrorodorsal) designed to preserve columnar connections in the somatosensory cortex were prepared in ice-cold artificial CSF (ACSF) containing the following (in mM): 119 NaCl, 2.5 KCl, 1 NaH_2PO_4 , 26.2 NaHCO_3 , 11

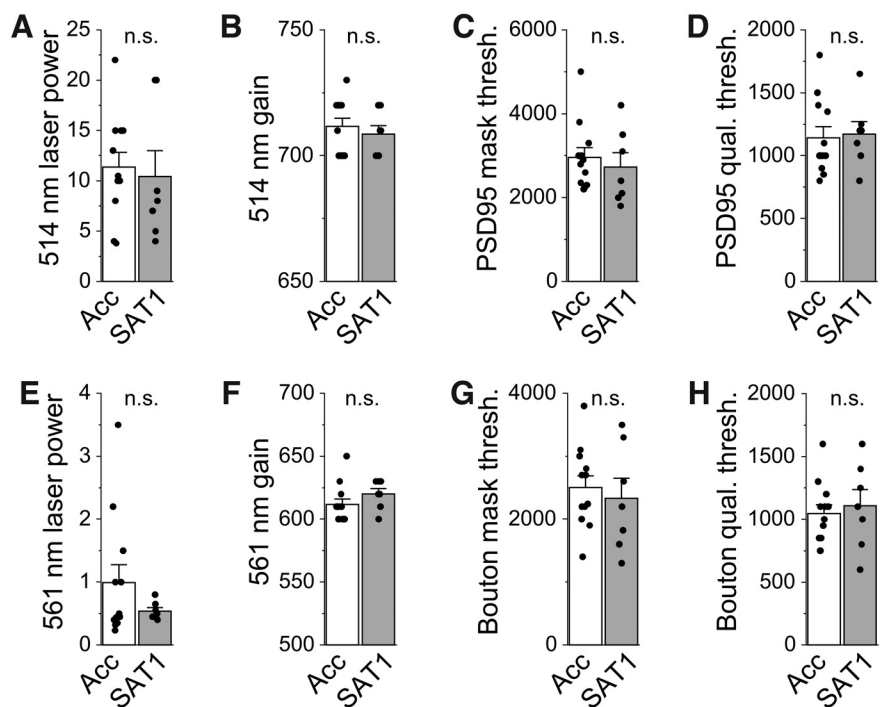


Figure 3. Imaging and analytical parameters do not differ between experimental groups. All comparisons were made for L5a images from individual animals from acclimation control (Acc; white) and SAT1 (gray) experimental groups. **A–F**, Each dot represents value for individual animal \pm SEM; bar graphs represent mean \pm SEM. $N = 12$ Acc and 7 SAT1 mice. **A**, Laser intensities for excitation of PSD95.FingR-Citrine fluorescence. Unpaired $t_{(17)} = 0.34$; $p = 0.74$. **B**, Camera gain setting for acquiring PSD95.FingR-Citrine fluorescence. Unpaired $t_{(17)} = 0.62$; $p = 0.54$. **C**, Imaris watershed algorithm threshold for reconstructing PSD95.FingR-Citrine puncta contours. Unpaired $t_{(17)} = 0.58$; $p = 0.57$. **D**, Imaris object-splitting algorithm threshold for separating fused PSD95.FingR-Citrine puncta. Unpaired $t_{(17)} = -0.22$; $p = 0.83$. **E**, Laser intensities for excitation of tdTomato-labeled POM bouton fluorescence. Unpaired $t_{(17)} = 1.19$; $p = 0.25$. **F**, Camera gain setting for acquiring tdTomato-labeled POM bouton fluorescence. Unpaired $t_{(17)} = -0.124$; $p = 0.23$. **G**, Imaris watershed algorithm threshold for reconstructing tdTomato-labeled POM bouton contours. Unpaired $t_{(17)} = 0.50$; $p = 0.62$. **H**, Imaris object-splitting algorithm threshold for separating fused tdTomato labeled POM bouton. Unpaired $t_{(17)} = -0.45$; $p = 0.66$.

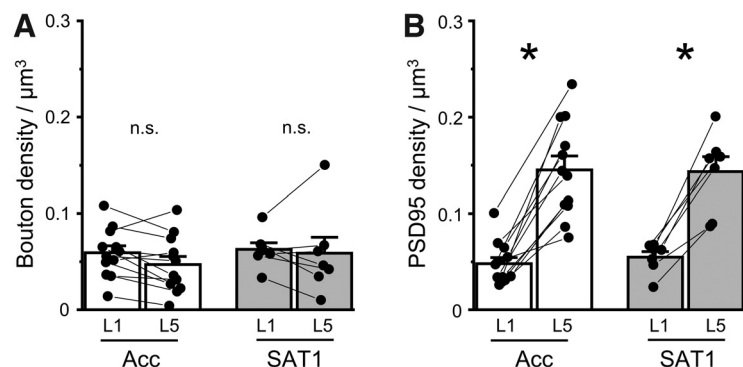


Figure 4. Density of axonal bouton and postsynaptic labeling is comparable across control and trained animals. **A**, Within (connected lines) and across-animal comparisons for densities of digitally detected POM boutons in L1 and L5a from acclimation control (Acc) and trained (SAT1) mice. Bouton density was not significantly different between L1 and L5a within layers or across training. Statistical difference was assessed using two-way repeated-measures ANOVA followed by *post hoc* Tukey's test for comparisons across layers and across training if ANOVA results were significant, $F_{(1,17)} = 2.35$; $p = 0.14$. **B**, As in **A** but for PSD95 puncta density. PSD95 puncta density was significantly higher in L5a than L1 for both Acc and SAT1 animals, $F_{(1,17)} = 102.5$; $p = 1.29 \times 10^{-8}$. Tukey's $p(\text{across-layer}) = 4.17 \times 10^{-7}$; Tukey's $p(\text{across-group}) = 0.83$. Bar graphs represent mean \pm SEM; $N = 12$ Acc and 7 SAT1 mice.

glucose, 1.3 MgSO_4 , and 2.5 CaCl_2 equilibrated with 95%/5% O_2/CO_2 . Slices were allowed to recover for 1 h at room temperature in the dark before recording. The injection site was confirmed anatomically using the eYFP-tagged ChR2 fluorescence characteristic pattern of L1 and L5a fluorescent axonal labeling in the barrel cortex. Slices that had fluorescently labeled axons outside the target layers were discarded.

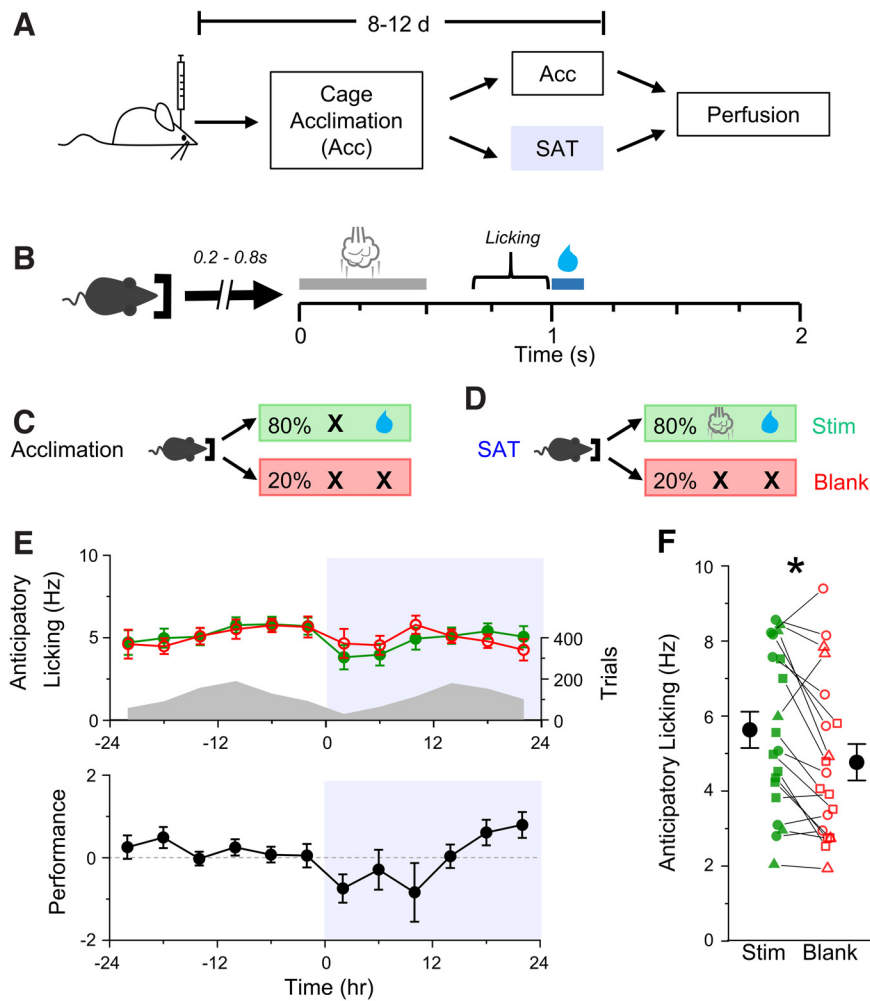


Figure 5. SAT in virally transduced transgenic mice. **A**, Schematic demonstrating the timeline of viral injection, training, and perfusion of mice. Cage acclimation control (Acc) preceded SAT by at least 24–48 h. **B**, Trial structure for sensory training. Nose poking triggers trial onset with a random variable delay. **C**, Contingency table during the acclimation condition showing that mice receive a water reward (no stimulus) in 80% of the trials and nothing (no stimulus and no reward) in the remaining 20% of the trials. **D**, Same as in **C**, but during SAT, 80% of trials have an air-puff stimulus followed by water delivery, and 20% of trials have no stimulus and no reward (blank). Stimulus, Stim. **E**, Summary of anticipatory licking behavior of mice for 24 h before and after the onset of SAT (time = 0 h, blue shaded region). Top, Anticipatory lick rates for Stim water (green) and blank (red) trials. The averaged number of trials across time bins is shown in gray. Bottom, Performance ($L_{\text{Stim}} - L_{\text{Blank}}$) across time, $N = 20$ mice. **F**, Mean anticipatory licking is significantly increased for Stim (green) versus Blank (red) trials for the last 20% of trials at the end of the first training day. Paired $t_{(19)} = 3.11$; $p = 0.0058$. Individual animal licking records on the first day of training are marked by connected points using different shapes for differing SAT group identities; circles for SAT1, triangles for SAT2, and squares for SAT5. Black symbols represent group mean \pm SEM; $N = 20$ mice.

Electrophysiology. L5 Pyr were targeted for whole-cell recording in the posteromedial barrel subfield using an BX51WI light microscope (Olympus) with borosilicate glass electrodes resistance 4–8 M Ω at room temperature. Electrode internal solution for qEPSCs recordings contained the following (in mM): 130 cesium gluconate, 10 HEPES, 0.4 EGTA, 2.8 NaCl, 10 TEA, 4 Mg-ATP, and 0.4 Na-GTP, pH 7.25–7.30, 280–290 mOsm, and typically contained QX-314 (5 mM; lidocaine *N*-ethyl bromide, Tocris Bioscience). Trace amounts of Alexa Fluor 568 were added to the internal solution to confirm pyramidal cell morphology. Electrophysiological data were acquired using a MultiClamp 700A amplifier (Molecular Devices) and a National Instruments acquisition interface. Data were filtered at 3 kHz, digitized at 10 kHz, and collected by Igor Pro 6.37 software (WaveMetrics). Cells were allowed to recover from break in for 3 min before data collection. R_s and R_i were monitored for the duration of experiments, and cells with $R_i < 100$ M Ω , $R_s > 35$ M Ω , or where R_s changed by $>30\%$ over the course of data collection were excluded from further analysis. Cells

from both groups had similar mean values of V_{rest} , capacitance, and series and input resistance.

Quantal amplitude measurements were performed in the standard ACSF solution using during cutting, wherein 2.5 mM CaCl_2 was replaced with SrCl_2 , and the NMDA receptor antagonist AP-5 (50 μM ; catalog #HB0225, Hello Bio) was included in the bath solution. Well-isolated qEPSCs were recorded at -70 mV following optical stimulation (one pulse, variable intensity) to activate ChR2-expressing POM axons (Audette et al., 2019). Analysis was performed blind to experimental condition. Quantal events were manually confirmed based on their short rise time, isolated baselines, and absence of multiple inflection points indicative of a compound event. Events occurring between 50 and 500 ms following stimulation (≥ 25 per cell) were analyzed using MiniAnalysis software (Synaptosoft) after applying a low-pass elliptic filter at 1 kHz. Detection parameters used were the following: threshold 9 pA, local maximum period 3.5 ms, baseline period 6 ms, decay time period 10 ms, decay time fraction 0.333, baseline average period 4 ms; area threshold 10 pA, peak average points 3). Individual qEPSCs were aligned to rise and averaged to generate an average qEPSC trace for each cell. The cell average qEPSC trace for each cell was then aligned to rise and averaged to generate a global qEPSC mean trace for each group. The amplitude of each event was averaged to determine the average qEPSC amplitude of a cell, and cumulative distribution histograms were generated from a pool of qEPSCs containing 25 randomly selected events from individual cell within each experimental group.

Experimental design and statistical analyses. All statistical tests and graphing were performed with OriginPro (version 2022, OriginLab). Stereotactically injected animals were randomly assigned to either the acclimation control or SAT training groups. To leverage the large numbers of measurements per animal (synapses/qEPSCs), comparisons were made using cumulative distribution histograms where the number of observations was randomly selected and balanced across animals. Briefly, the spatial order of puncta in an ROI was shuffled, and a defined number of puncta balanced across animals were selected for size differences using cumulative distribution plots. For axonal boutons, the FOV generated thousands of presynaptic structures (boutons and some interbouton segments). High-fidelity boutons from selected segments ranged from 85 to 119 per sample. Animals with substantially fewer boutons and PSD95 puncta in the FOV analyses were excluded from the cumulative distribution plots to maximize and balance the number of observations. Specifically, a single animal was dropped from the acclimation control group and also the SAT1 group of mice because of lower numbers of either POM axons or PSD95 puncta labeled in the FOVs with anatomic overlap of labeling.

Cumulative distribution histograms were compared using Kolmogorov–Smirnov (K–S) tests. For bar graphs, all values for a given measurement within an animal were averaged and then averaged for all subjects within a group. Values are mean \pm SEM, unless otherwise indicated. Differences across animal groups within layers were tested

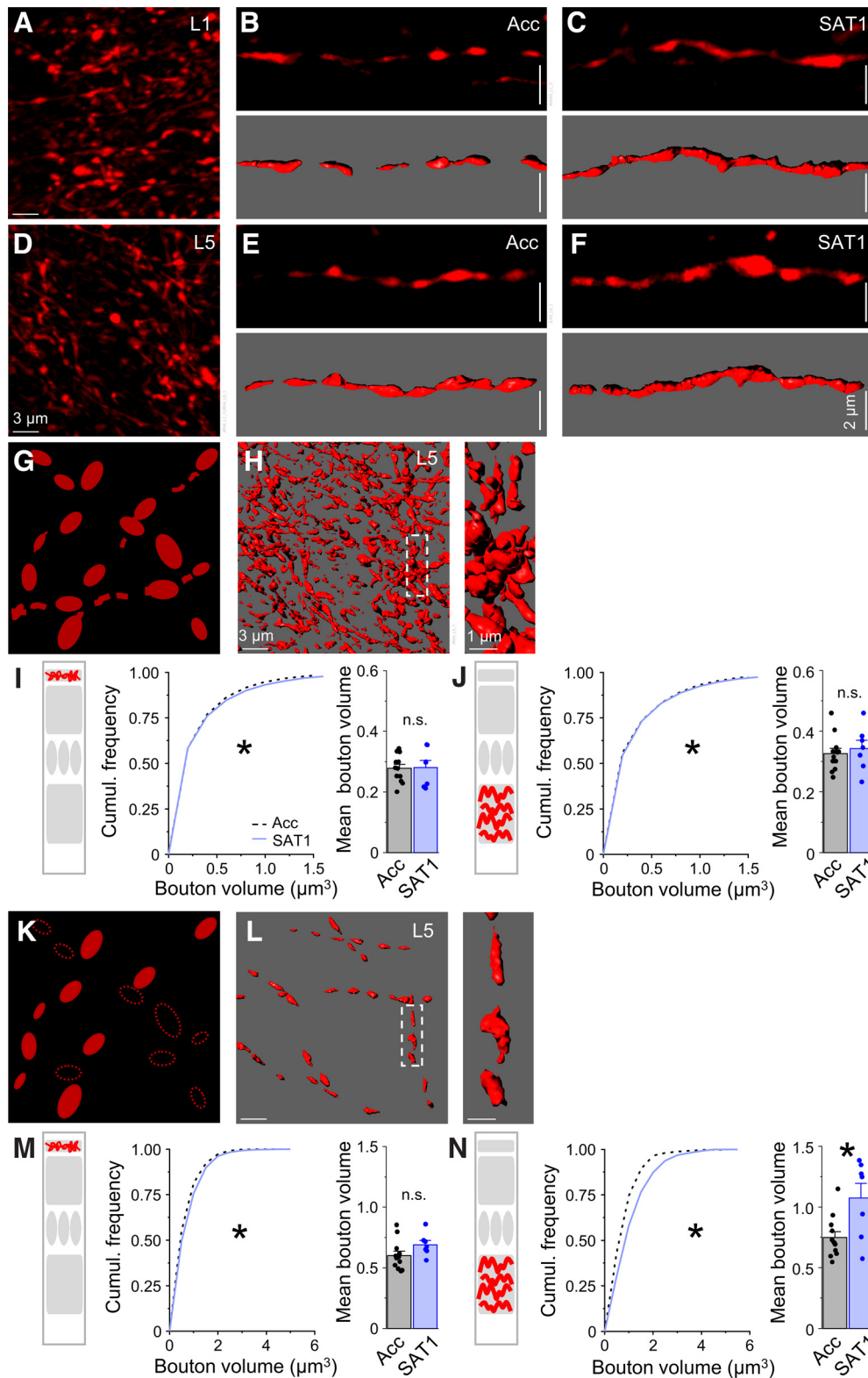


Figure 6. POM bouton size selectively increases in L5a at the onset of training. **A**, Image of an optical stack showing tdTomato-labeled POM boutons in L1 from S1 barrel cortex of an acclimation control (Acc) mouse. **B**, **C**, Images of individual axon segments in L1 from **B**, an Acc animal (top, tdTomato fluorescence; bottom, reconstruction), and **C**, SAT1 trained animal. **D**, Same as in **A** but from L5a. **E**, Same as in **B** but from L5a. **F**, Same as in **C** but from L5a. **G**, Diagram showing reconstructed presynaptic boutons in an FOV. Note the occasional inclusion of interbouton segments either fused to or independent of nearby boutons. **H**, POM boutons reconstructed in Imaris from the FOV in **D**, with a zoomed image of the boxed boutons on the right. **I**, Left, Schematic showing POM boutons in L1. Middle, Cumulative distribution histogram of randomly selected POM bouton volumes pooled across L1 FOVs from Acc (dashed black line; 22,000 boutons; 11 mice) and SAT1 (blue line; 12,000 boutons; 6 mice) animals. K–S test, $p = 0.0058$. Right, Animal averaged mean bouton volume + SEM by animal (solid dots); $N = 12$ Acc and 7 SAT1 mice. Unpaired $t_{(17)} = -0.11$; $p = 0.91$. **J**, Same as in **I** but for L5a FOVs. Left, Schematic showing POM boutons in L5a. Middle, Cumulative distribution histogram of POM bouton volumes pooled across L5a FOVs from Acc (dashed black line; 22,000 boutons; 11 mice) and SAT1 (blue line; 12,000 boutons; 6 mice) mice. K–S test, $p = 0.018$. Right, Animal averaged mean bouton volume + SEM by animal (solid dots); $N = 12$ Acc and 7 SAT1 mice. Unpaired $t_{(17)} = -0.54$; $p = 0.59$. **K**, Schematic of reconstructed and selected POM axonal segments. **L**, POM axonal

using unpaired *t* test for two groups and one-way ANOVA followed by *post hoc* Tukey's tests for analyses across multiple time-points; $p < 0.05$ was considered for assessing statistical significance. Power analyses were not conducted. Statistical analyses were not segregated by sex as a biological variable because of significant loss in statistical power and are beyond the scope of this study.

Results

Association learning is heterogeneous across animals

SAT rapidly drives changes in thalamocortical synaptic strength (Audette et al., 2019), providing an excellent experimental system to evaluate and deploy fluorescence-based synapse detection and analysis for discovery. Virally transduced Rbp4-Cre mice were either housed in the training cage (acclimation controls) or underwent sensory association training (SAT; Fig. 5). Similar to experiments in wild-type animals (Audette et al., 2019; Bernhard et al., 2020), slightly more than half of trained animals showed an increase in stimulus-associated anticipatory licking after a single day of training (SAT1; Fig. 5E,F). This change was linked to both an increase in stimulus-associated licking and a reduction in licking to blank trials within the 24 h training period. Thus, viral expression in this transgenic background did not alter learning behavior.

Boutons increase in size during early sensory learning

POM axons innervating the barrel cortex have dense terminations in both L5a and L1, innervating both excitatory and inhibitory neurons in deep and superficial layers of the cerebral cortex (Wimmer et al., 2010; Audette et al., 2018). We thus targeted these layers for reconstruction and quantitative analyses (Fig. 2). Electrophysiological studies have shown that POM-qEPSCs in L5a Pyr neurons inputs rapidly increase in amplitude after a single day of SAT (Audette et al., 2019). However, the somatodendritic location of these potentiated synapses cannot be easily inferred from electrophysiological studies. Although space-clamp constraints suggest that qEPSCs from proximal synapses were most likely detected during whole-cell recordings, prior imaging studies suggest that synapses in L1 may be modified by experience and learning (Fu et al., 2012; Kuhlman et al., 2014; Chen et al., 2015; Lacefield et al., 2019; Graves et al., 2021). Thus, it was unknown whether SAT-dependent synaptic potentiation would occur broadly across the somatodendritic arbor of the L5 Pyr or might be restricted to one domain.

To compare SAT-dependent changes in POM boutons in different cortical layers, we used an FOV analysis to detect and compare bouton volume where thousands of observations could be detected in a given specimen (Fig. 6). Cumulative distribution histograms were constructed to compare bouton volume across conditions. Using thousands of bouton measurements per animal, we observed a small but significant shift in

bouton volume within both layers after a single day of training, but this difference was not apparent when bouton volumes were averaged across animals (control vs SAT1 in L1, 0.28 ± 0.01 vs $0.28 \pm 0.02 \mu\text{m}^3$; control vs SAT1 in L5a, 0.33 ± 0.02 vs $0.34 \pm 0.03 \mu\text{m}^3$; Fig. 6G–J).

Because our semiautomated FOV reconstructions capture both boutons and occasional smaller fragments of interbouton segments that can dilute out potential differences, we also selected individual POM axonal segments (5–12 contiguous boutons long) from each animal for reconstruction (Fig. 6K,L). Although this analysis captured fewer boutons than the FOV analysis, data were generally of higher quality because interbouton segments that were unlikely to be release sites could be excluded from reconstruction and analysis. Importantly, axonal segments were selected blind to experimental condition. Axonal segment analysis revealed a significant rightward shift in the distribution of POM bouton sizes for L5a and L1 after 1 d of SAT, a difference that was also reflected in an apparent 15% increase in L1 mean bouton size and a significant 40% increase in L5a mean bouton size averaged across animals (control vs SAT1 in L1, 0.60 ± 0.03 vs $0.69 \pm 0.04 \mu\text{m}^3$; control vs SAT1 in L5a, 0.75 ± 0.05 vs $1.07 \pm 0.12 \mu\text{m}^3$; Fig. 6M,N). Because POM axons target Pyr neurons in both L5 and L2 as well as inhibitory interneurons (Audette et al., 2018), the postsynaptic target of individual boutons could not be determined. However, these layer-specific changes in bouton size—most prominent in L5a—suggest that fluorescence-based anatomic analyses can provide sufficient resolution to detect experience-dependent changes in synaptic properties and facilitate biological insights into mechanisms of neural circuit plasticity.

Fluorescence-based synaptic detection facilitates analysis of large numbers of animals, enabling us to evaluate potential correlations between learning behavior and anatomic changes. The heterogeneity in both POM bouton size and stimulus-associated licking after 1 d of SAT suggested that there might be a correlation between behavior and POM measurements. However, this was not the case; POM bouton size was not correlated with behavioral change for individual animals in either layer (L1, Pearson's $r = -0.037$, $p = 0.94$; L5a, Pearson's $r = 0.43$, $p = 0.33$; $N = 7$).

Excitatory synaptic changes in L5 Pyr neurons

PSD95 is a marker for excitatory synapses in the neocortex, and changes in postsynaptic levels of PSD95 can serve as a postsynaptic indicator of synaptic plasticity (Ehrlich and Malinow, 2004; Meyer et al., 2014; Hruska et al., 2018). PSD95.FingR expression in L5 Pyr neurons enabled us to evaluate SAT-associated changes in excitatory synapses using the punctate Citrine fluorescence linked to FingR (Fig. 7). FOV analyses captured all PSD95-tagged excitatory synapses on L5 Pyr neurons, only some of which will correspond to thalamocortical inputs (Schoonover et al., 2014; Bopp et al., 2017; Kim et al., 2022). This analysis could also focus on either the proximal (L5a) or apical (L1) dendritic compartments of L5 Pyr neurons to determine where within the cortical column synaptic changes might occur during training. Cumulative distribution plots of thousands of PSD95 puncta showed a small but highly significant shift in the size distribution of puncta between control and SAT1 animals (Fig. 7A–E). In L1, PSD95 puncta were marginally smaller. In contrast, puncta were significantly larger in L5a. These differences were also visible in across-animal averages, although not significant, likely because of heterogeneity in mean puncta size measurements across

←

segments containing 5–12 contiguous boutons were randomly selected from the FOV reconstructions in **H**. Interbouton segments were deleted from the reconstructions. **M**, Left, Schematic of POM boutons from selected axonal segments in L1. Middle, Cumulative distribution histogram from Acc (dashed black line; 960 boutons; 12 mice) and SAT1 (blue line; 560 boutons; 7 mice) animals. K–S test, $p = 0.012$. Right, Animal-averaged mean bouton volume + SEM by animal (solid dots); $N = 12$ Acc and 7 SAT1 mice. Unpaired $t_{(17)} = -1.68$; $p = 0.11$. **N**, Left, Schematic for L5a POM boutons. Middle, Cumulative distribution histogram from Acc (dashed black line; 960 boutons; 12 mice) and SAT1 (blue line; 560 boutons; 7 mice) animals. K–S test, $p = 3.87 \times 10^{-9}$. Right, Averaged mean bouton volume + SEM by animal (solid dots); $N = 12$ Acc and 7 SAT1 mice. Unpaired $t_{(17)} = -2.95$; $p = 0.009$.

animals (L1, control 1.54 ± 0.08 vs SAT1 $1.51 \pm 0.10 \mu\text{m}^2$; L5a, control 1.28 ± 0.05 vs SAT1 $1.39 \pm 0.08 \mu\text{m}^2$).

L5 Pyr neurons receive diverse excitatory input from columnar, thalamocortical, and corticocortical sources, and FOV analysis of all PSD95 puncta cannot differentiate between input sources. Because L5 Pyr neurons receive strong local and also long-range inputs, the vast majority of PSD95 puncta are likely to originate from nonthalamic excitatory inputs. Indeed, prior anatomic studies suggest that only $\sim 15\%$ of excitatory synapses in L4 come from thalamic inputs (Schoonover et al., 2014).

To determine whether these effects might be concentrated in POM-associated synapses, we restricted our analysis to PSD95 puncta that had been digitally aligned to all detected POM axonal boutons reconstructed from the entire FOV. Similar to the effects observed for all PSD95 puncta, we observed a small reduction in size for L1 synapses and a larger and highly significant increase in size for L5a synapses in the cumulative distribution histograms that was also reflected in the across-animal averages (L1, control 1.92 ± 0.10 vs SAT1 $1.91 \pm 0.09 \mu\text{m}^2$; L5a, control 1.71 ± 0.09 vs SAT1 $1.80 \pm 0.10 \mu\text{m}^2$; Fig. 7F–J).

Although prior *in vivo* imaging studies have detected learning-related changes in the dynamics of dendritic spines in neocortical L1 including the addition and stabilization of a small number of dendritic spines (Yang et al., 2009; Kuhlman et al., 2014; Chen et al., 2015), this was not visible via population analysis of L1-localized, PSD95-tagged thalamocortical synapses on the apical dendrites of L5 Pyr neurons. Together, these data suggest that L5a but not L1 is the site for increases in excitatory synaptic size during acquisition of a sensory learning task.

Validation of POM-L5 synaptic contacts

Digital alignment of presynaptic and postsynaptic elements from fluorescently labeled images can be inaccurate because the synaptic cleft is almost an order of magnitude smaller than the diffraction limit of light in our confocal images. To estimate what fraction of the digitally identified synapses were likely to be true positives, we evaluated a subset of reconstructed axonal segments that had been aligned to PSD95 puncta and then immunostained for a third factor for synapse identification, the presynaptic marker Bassoon. Bassoon is ubiquitous at vesicles within the presynaptic terminal (Dresbach et al., 2001) and is commonly used as a marker for central synapses (Kuljis et al., 2019; Moreno Manrique et al., 2021). Digitally

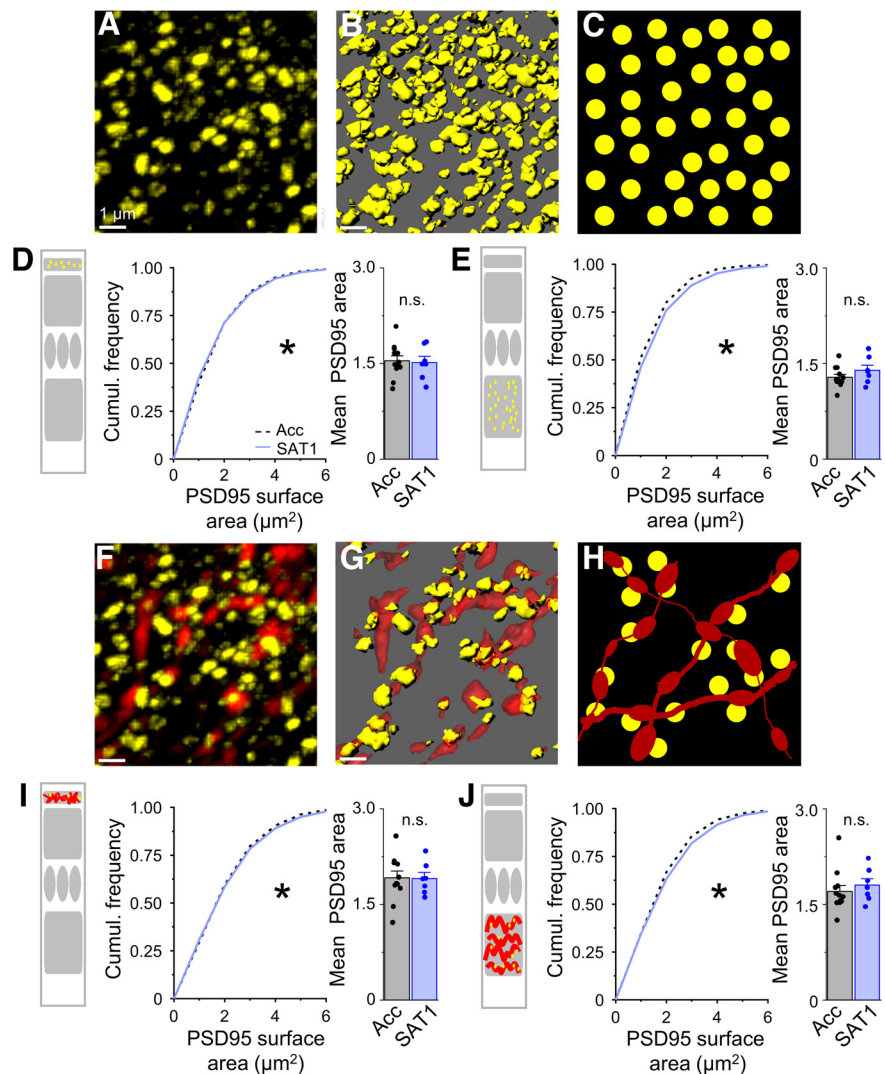


Figure 7. SAT drives compartment-specific changes in PSD95 puncta on L5 Pyr dendrites. **A**, Image of an optical stack showing Citrine-labeled PSD95.FingR puncta in L5a from S1 barrel cortex from an acclimation control (Acc) mouse. **B**, All PSD95 puncta reconstructed from FOV in **A**. **C**, Schematic showing an FOV of reconstructed PSD95.FingR puncta (yellow). **D**, Left, Schematic showing PSD95.FingR puncta in L1. Middle, Cumulative distribution histogram of randomly selected L1 PSD95.FingR puncta from Acc (dashed black line; 6600 puncta; 11 mice) and SAT1 (blue line; 3600 puncta; 6 mice) animals. K–S test, $p = 0.015$. Right, Averaged mean puncta surface area \pm SEM by animal (solid dots); $N = 12$ Acc and 7 SAT1 mice. Unpaired $t_{(17)} = 0.23$; $p = 0.82$. **E**, Same as in **D** but for L5a FOV. Left, Schematic showing PSD95.FingR puncta in L5a. Middle, Cumulative distribution histogram of randomly selected L5a PSD95.FingR puncta from Acc (dashed black line; 11,000 puncta; 11 mice) and SAT1 (blue line; 6000 puncta; 6 mice) animals. K–S test, $p = 2.65 \times 10^{-10}$. Right, Averaged mean puncta surface area \pm SEM by animal (solid dots); $N = 12$ Acc and 7 SAT1 mice. Unpaired $t_{(17)} = -1.29$; $p = 0.021$. **F**, As in **A** but with tdTomato-labeled POM axons. **G**, As in **B** but showing only digitally detected PSD95 puncta (yellow) contacting POM axons (red). **H**, Schematic showing puncta touching POM axons. Note the inclusion of interbouton segments either fused to or independent of the nearby boutons. **I**, As in **D** but for POM-assigned PSD95 puncta in L1 (left). Middle, Cumulative distribution histogram of randomly selected puncta from Acc (dashed black line; 6600 puncta; 11 mice) and SAT1 (blue line; 3600 puncta; 6 mice) animals. K–S test: $p = 0.0031$. Right, Averaged mean puncta surface area \pm SEM by animal (solid dots); $N = 12$ Acc and 7 SAT1 mice. Unpaired $t_{(17)} = 0.066$; $p = 0.95$. **J**, As in **I** but for POM-assigned PSD95 puncta in L5a (left). Middle, Cumulative distribution histogram of randomly selected L5a PSD95.FingR puncta from Acc (dashed black line; 11,000 puncta; 11 mice) and SAT1 (blue line; 6000 puncta; 6 mice) animals. K–S test, $p = 3.78 \times 10^{-6}$. Right, Averaged mean puncta surface area \pm SEM by animal (solid dots); $N = 12$ Acc and 7 SAT1 mice. Unpaired $t_{(17)} = -0.68$; $p = 0.50$.

detected synapses that also contained Bassoon immunolabeling are likely to be true positives; detected synapses that lack Bassoon in the presynaptic compartment might be false positives.

Because antibody staining is heavily influenced by tissue permeability, analysis was restricted to the top of the specimen where immunostaining was strong. As expected by the density of cortical synapses observed in EM analysis, Bassoon labeling was ubiquitous across the specimen (Fig. 8A). Expression of virally

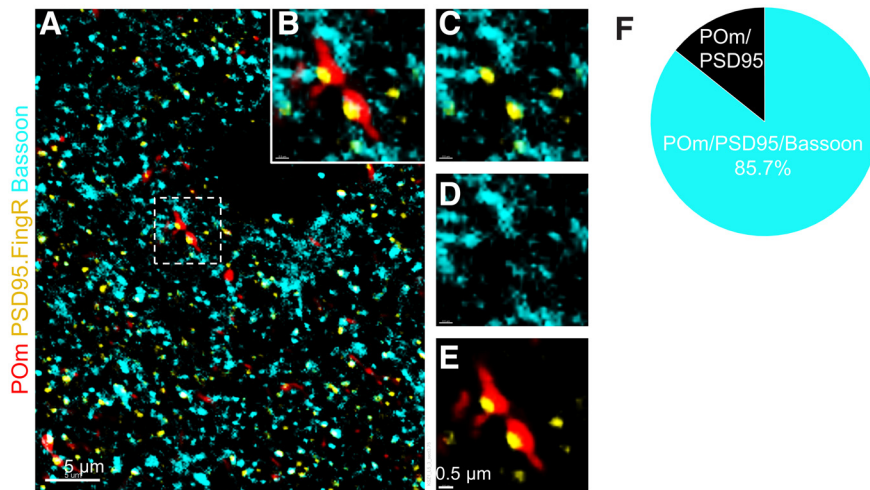


Figure 8. Validation of digitally detected synapses using presynaptic Bassoon immunolabeling. **A**, L5a in barrel cortex from a virally transduced acclimation control mouse with PSD95.FingR puncta (yellow), POM axons (red), and Bassoon immunostaining (cyan). **B**, Zoomed image from **A** (dashed box) showing a pair of POM-assigned PSD95 puncta with Bassoon immunolabeling at the interface of PSD95.FingR and POM bouton apposition. **C**, PSD95.FingR and Bassoon fluorescent overlay. **D**, Bassoon immunolabeling. **E**, POM bouton and PSD95.FingR fluorescence overlay. **F**, The fraction of detected POM-assigned PSD95 puncta that were Bassoon positive or Bassoon negative ($n = 77$ putative contacts from 2 acclimation control mice).

transduced fluorescent labels for thalamic boutons and cortical PSD95 was more uniform across the tissue section than immunolabeling and enabled analysis deeper into the sample, an important advantage of these genetically encoded synaptic tags.

The majority (>85%) of PSD95 puncta associated with POM boutons aligned with Bassoon immunoreactivity that was both within the bouton and directly adjacent to the detected PSD95 contact, reflecting the expected spatial organization of Bassoon within the presynaptic terminal and active zone in line with the postsynaptic structure (Fig. 8B–F). Although Bassoon staining was punctate throughout the labeled area, we observed that thalamocortical boutons rarely showed strong punctate immunolabeling. A minority of putative contacts showed no detectable Bassoon immunoreactivity (~2%). It is likely that immunostaining cannot detect Bassoon that is expressed at low levels; however, it is also possible that some boutons lacking Bassoon may use other molecules to compensate for its function. This is consistent with prior studies suggesting that Bassoon may be absent at some synapses, including VGLUT-2-expressing synapses (Micheva et al., 2010; Heise et al., 2016). However, it is likely that some putative contacts lacking Bassoon are false positives. Overall, we conclude that the vast majority of PSD95 puncta that are aligned with POM boutons are likely to be true synaptic contacts.

Because our labeling strategy is nonsaturating and indeed showed substantial variability across animals (Fig. 4), it is likely there are many bona fide POM synapses onto L5 Pyr neurons that were not detected in our analysis. This false-negative rate could not be easily assessed as immunohistochemical markers for thalamocortical synapses are not comprehensive (e.g., VGLUT-2 is not equally expressed in all thalamocortical synapses in S1; Graziano et al., 2008), and even immuno-EM approaches will not label all proteins present.

Layer-specific changes in POM-associated PSD95 puncta during learning

Our initial survey used POM boutons detected from an entire FOV, an approach that could sometimes include interbouton

segments or aberrantly fragmented/fused boutons. Bouton reconstruction from selected axonal segments yielded a higher-quality dataset that revealed more pronounced changes in bouton morphology (Fig. 6K–N) and were thus used for digital detection of closely associated PSD95 puncta (<0.15 μm) as these were most likely to represent thalamocortical synapses (Fig. 9). In L1, the fraction of excitatory synapses from POM versus other sources may be higher than in L5a, although these apical dendrites also receive inputs from diverse brain areas (Schuman et al., 2021; Kim et al., 2022). After 1 d of SAT and similar to the FOV analysis of PSD95 puncta, POM-assigned PSD95 puncta in L1 were reduced in size compared with control mice, showing a significant leftward shift in their distribution and a significant 20% decrease in mean size averaged across animals (control 2.14 ± 0.10 vs SAT1 $1.78 \pm 0.07 \mu\text{m}^2$; Fig. 9I).

In contrast, after 1 d of SAT, POM-associated PSD95 puncta in L5a showed a significant increase in size with a pronounced rightward shift in distribution in the cumulative distribution. Averaged across animals, this represented an increase of ~14% (control 1.71 ± 0.06 vs SAT1 $1.94 \pm 0.12 \mu\text{m}^2$), an increase that was more than two-fold greater than what was observed when all PSD95 puncta in a FOV were analyzed (Fig. 9J).

Because of limitations inherent in fluorescence microscopy, the 0.15 μm threshold was well above the actual distance between presynaptic elements and thus would include some false positives, that is, non-POM-associated puncta. Because of this, we estimate that the actual increase in POM synapses may be substantially larger as local excitatory inputs within L5 were not functionally altered after SAT (Audette et al., 2019). These anatomic data are consistent with electrophysiological studies demonstrating rapid increases in POM but not intracortical qEPSCs in L5 Pyr at the onset of training (Audette et al., 2019). Thus, focused analysis of input-specific postsynaptic sites can reveal training-induced increase in synapse size.

Selective analyses of PSD95 puncta that are closely associated with POM axonal boutons reveal pronounced and layer-specific changes after SAT, amplifying effects that were observed in FOV analysis. The fact that small changes observed in FOV analysis (where all presynaptic and postsynaptic objects were digitally detected and aligned) were amplified by selective analysis of boutons along contiguous axonal segments (a smaller but higher-quality dataset) shows that high-throughput analyses can provide insight into circuit reorganization during learning. In addition, these data suggest that SAT drives a reweighting of thalamocortical input onto L5 Pyr neurons, where POM inputs to L5a become more powerful compared with POM inputs arriving at L1 dendrites.

Because data were collected from both L1 and L5a in the same animal, we could compare the thalamocortical synapses across layers within an animal, providing a control for viral transduction or behavioral variability between subjects. Within-animal comparisons showed that PSD95 size was significantly larger in L1 than in L5a in control animals (L1 2.14 ± 0.11 vs L5 $1.71 \pm 0.06 \mu\text{m}^2$; paired $t_{(11)} = 3.56$; $p = 0.0044$), consistent with prior

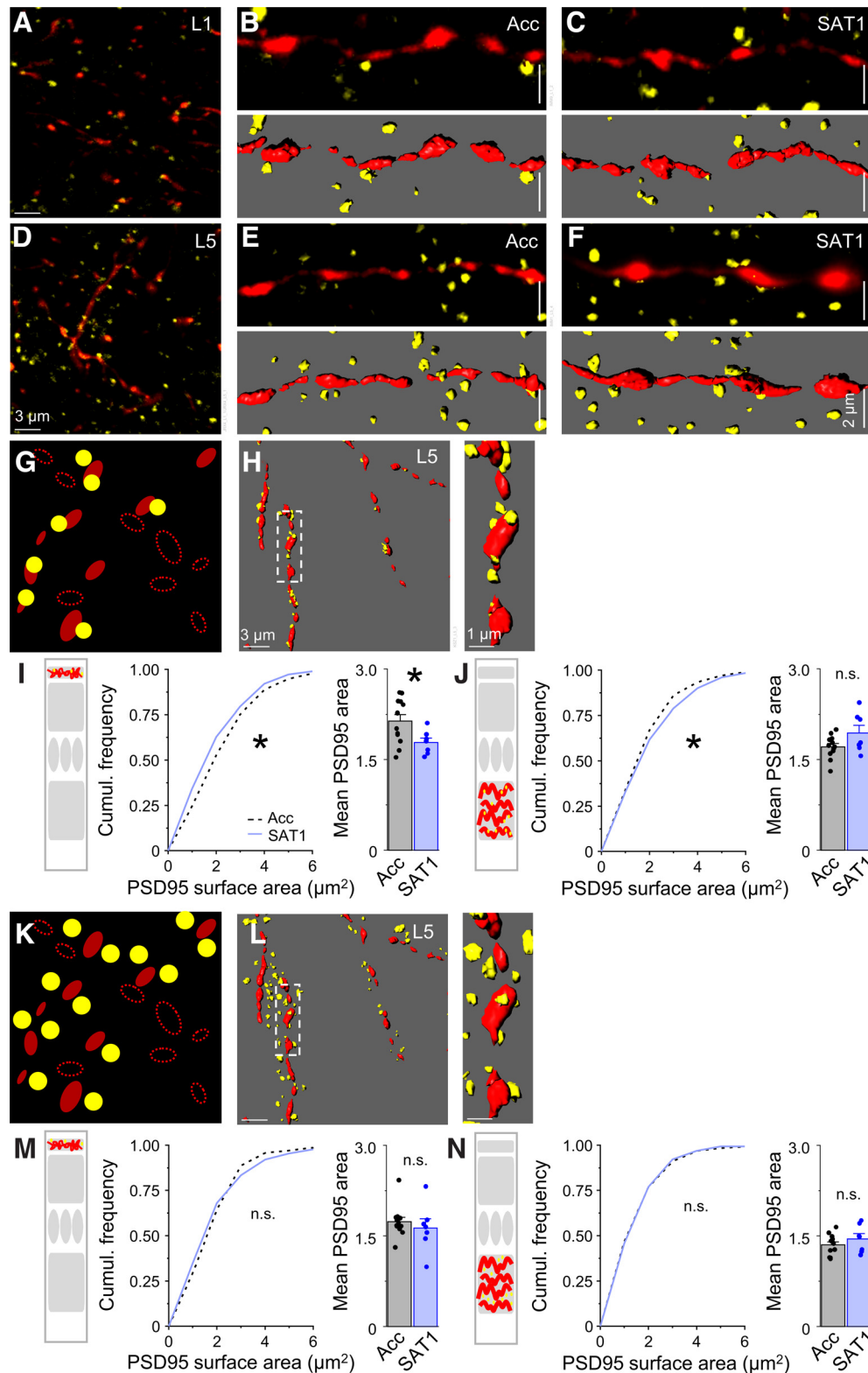


Figure 9. Layer-specific increase in P0m synaptic size during sensory learning. **A**, Image of an optical slice from L1 in barrel cortex with PSD95.FingR puncta (yellow) and P0m axons (red) from virally transduced Rbp4-Cre transgenic acclimation control (Acc) mouse. **B**, Individual P0m axon segments with adjacent PSD95 puncta in L1 from an Acc animal (top, tdTomato fluorescence; bottom, reconstruction). **C**, Same as in **B** but from L1 of an SAT1 trained mouse. **D–F**, Same as in **A–C** but from L5a. **G**, Schematic showing verified reconstructions of axonal boutons within a contiguous segment (filled red symbols). Yellow circles indicate digitally detected PSD95 puncta that are touching P0m boutons, that is, P0m-assigned PSD95 puncta. **H**, Digital rendering of randomly selected axonal segments and assigned PSD95 puncta from a representative L5a image. Right, Zoom of boxed segment. **I**, Left, Schematic of P0m-assigned PSD95 puncta in L1. Middle, Cumulative distribution histogram of P0m-assigned synapses in L1 showing a reduction in synaptic size after training from Acc (dashed black line; 300 puncta; 12 mice) and SAT1 (blue line; 175 puncta; 7 mice) animals. K–S test, $p = 0.042$. Right, Averaged mean puncta surface area + SEM by animal (solid dots); $N = 12$ Acc and 7 SAT1 mice. Unpaired $t_{(17)} = 2.31$; $p = 0.034$. **J**, Left, Schematic of P0m-assigned PSD95 puncta in L5a. Middle, Cumulative distribution histogram of P0m-assigned synapses in L5a showing an increase in synaptic size after training from Acc (dashed black line; 720 puncta; 12 mice) and SAT1 (blue line; 420 puncta; 7 mice) animals. K–S test, $p = 0.024$. Right, Averaged mean puncta surface area + SEM by animal

observations (Rodriguez-Moreno et al., 2020). However, this difference disappeared after 1 d of SAT because of an increase in the size of PSD95 puncta in L5a and a reduction of size in L1 ($L1\ 1.78 \pm 0.07$ vs $L5\ 1.94 \pm 0.12\ \mu\text{m}^2$; paired $t_{(6)} = -1.27$; $p = 0.25$).

Finally, we used this dataset to investigate whether presynaptic and postsynaptic changes were well correlated at the onset of training. We asked whether the increase in PSD95 puncta size was most pronounced at the largest POM boutons, comparing PSD95 size in L5a for the largest 20% of POM boutons versus the mean for all POM-associated PSD95 puncta. However, there was no difference in the size of associated PSD95 puncta for the largest boutons compared with the group means (control 1.76 ± 0.07 vs SAT1 $1.88 \pm 0.15\ \mu\text{m}^2$), suggesting that plasticity mechanisms in presynaptic and postsynaptic compartments are not directly coordinated.

PSD95 puncta distant from POM axons do not show training-dependent changes in size

Digital analysis enables rapid sorting of PSD95 puncta based on their distance from detected POM axons. To assess whether the detected increase in POM-assigned synapses was specific for closely associated PSD95 puncta, we changed the criterion for digital detection of puncta that were more distant from the selected bouton (edge to edge, 0.5–1.0 μm ; Fig. 9K–N) but not touching other POM boutons. These more distant puncta are likely to mostly belong to other intracortical inputs, although a smaller fraction may receive inputs from POM axons that were not labeled in our experimental preparation.

Importantly, the SAT-associated change in PSD95 puncta size was not observed for these more distant objects in either L1 or L5a. Cumulative distribution histogram analyses showed no change in the size distribution of distant PSD95 puncta between control and SAT samples, also confirmed by comparing mean size across animals (L1, control 1.73 ± 0.07 vs SAT1 $1.63 \pm 0.15\ \mu\text{m}^2$; L5, control 1.35 ± 0.05 vs SAT1 $1.45 \pm 0.08\ \mu\text{m}^2$; Fig. 9M, N). This suggests that closely associated PSD95 puncta are specifically altered by SAT. These results indicate that despite limitations of fluorescence-based object localization, high-throughput detection and digital analysis can reveal statistically significant changes in input-specific synapses.

Structural changes in POM synapses are transient during learning

Prolonged training in this whisker-based sensory association task enhances stimulus-associated anticipatory licking and suppresses licking in blank trials, indicative of learning. To test whether these anatomic changes might be sustained

or enhanced across longer training periods, Rbp4-Cre animals with labeled POM axons and PSD95 synapses were subjected to 2–5 d of SAT, and the properties of POM boutons and POM-aligned PSD95 puncta were evaluated.

Animal performance, that is, the difference between licking in stimulus versus blank trials, progressively increased over 5 d of training (Fig. 10A,B), similar to what has been observed in prior studies (Lee et al., 2021). Analysis of reconstructed boutons from selected axonal segments after 2 and 5 d indicated that enlargement of POM boutons in L1 observed after SAT1 was reversed after extended training (control and SAT1 data from Fig. 6M; control, 0.60 ± 0.03 ; SAT1, 0.69 ± 0.04 ; SAT2, 0.60 ± 0.03 ; SAT5, $0.62 \pm 0.08\ \mu\text{m}^3$; Fig. 10C).

In L5a, the increase in bouton size at the onset of SAT was reduced after longer periods of training, showing a small but significant decrease compared with baseline levels in the cumulative distribution of bouton sizes, although this difference was not apparent in the across-animal mean (control and SAT1 data from Fig. 6N; control, 0.75 ± 0.05 ; SAT1, 1.07 ± 0.12 ; SAT2, 0.63 ± 0.07 ; SAT5, $0.65 \pm 0.04\ \mu\text{m}^3$; Fig. 10D).

PSD95 puncta associated with selected POM axonal segments showed a similar normalization back to baseline levels with extended training. The reduction in L1 PSD95 puncta size observed in the cumulative histogram analysis persisted for 2 d of SAT but returned to baseline levels by 5 d of SAT; but again these differences were not significant when averaged across animals (control and SAT1 data from Fig. 9I; control, 2.14 ± 0.1 ; SAT1, 1.78 ± 0.07 ; SAT2, 1.92 ± 0.20 ; SAT5, $2.17 \pm 0.14\ \mu\text{m}^2$; Fig. 10E). In L5a, POM-associated PSD95 puncta remained significantly larger after 2 d of SAT, returning to baseline levels after 5 d (control and SAT1 data from Fig. 9J; control, 1.71 ± 0.06 ; SAT1, 1.94 ± 0.12 ; SAT2, 1.92 ± 0.11 ; SAT5, $1.69 \pm 0.12\ \mu\text{m}^2$; Fig. 10F).

Structural markers predict functional strength of synapses

Do these anatomic changes correlate with functional synaptic strength of POM inputs onto L5 Pyr neurons? Prior whole-cell recording studies showed that a single day of SAT drove a significant increase in the amplitude of POM-evoked qEPSCs, a change that was maintained after 2 d of training (Audette et al., 2019). Prior studies did not assess whether this functional strengthening was maintained when animals became expert at the task. Our anatomic data predicts that the POM synaptic inputs onto L5 Pyr should renormalize after 5 d of training. To determine whether the anatomic result could predict electrophysiological strength of the synapse, we conducted additional electrophysiological recordings to assess qEPSC amplitude in acute brain slices from SAT5 tissue, using Chr2-mediated POM stimulation and whole-cell recording from L5a Pyr neurons (Fig. 11). Analysis was conducted blind to experimental condition. A comparison of age-matched control and 5 d SAT animals showed that thalamocortical qEPSC amplitudes were similar between the two groups (control 13.03 ± 0.42 vs SAT5 $13.22 \pm 0.37\ \text{pA}$; Fig. 11C,D), indicating that thalamocortical synaptic strength renormalized on extended training. These data indicate that the rapid changes in both presynaptic and postsynaptic anatomy induced by training in a sensory association task are transient, a finding corroborated by functional measurements. Importantly, the qEPSC measurements also confirm the validity and predictive power of our anatomic approach in assessing input-specific synaptic strength.

Discussion

Changes in either presynaptic or postsynaptic structures have been used to infer neural plasticity in a variety of brain areas.

←

(solid dots); $N = 12$ Acc and 7 SAT1 mice. Unpaired $t_{(17)} = -1.94$; $p = 0.068$. **K**, Schematic showing POM boutons with adjacent (0.5–1 μm), unassigned PSD95 puncta in L1. **L**, Digital rendering of randomly selected axonal segments and adjacent PSD95 puncta in L5a. Right, Zoom of boxed segment. **M**, Right, Schematic of POM-adjacent, unassigned PSD95 puncta in L1. Middle, Cumulative distribution histogram of adjacent POM synapses in L1 showing no change in synaptic size after training from Acc (dashed black line; 300 puncta; 12 mice) and SAT1 (blue line; 175 puncta; 7 mice) animals. K–S test, $p = 0.29$. Right, Averaged mean puncta surface area \pm SEM by animal (solid dots); $N = 12$ Acc and 7 SAT1 mice. Unpaired $t_{(17)} = 0.68$; $p = 0.51$. **N**, Left, Schematic of POM-adjacent, unassigned PSD95 puncta in L5a. Middle, Cumulative distribution histogram of adjacent synapses in L5a showing no change in synaptic size after training from Acc (dashed black line; 720 puncta; 12 mice) and SAT1 (blue line; 420 puncta; 7 mice) animals. K–S test, $p = 0.99$. Right, Averaged mean puncta surface area \pm SEM by animal (solid dots); $N = 12$ Acc and 7 SAT1 mice. Unpaired $t_{(17)} = -1.06$; $p = 0.30316$.

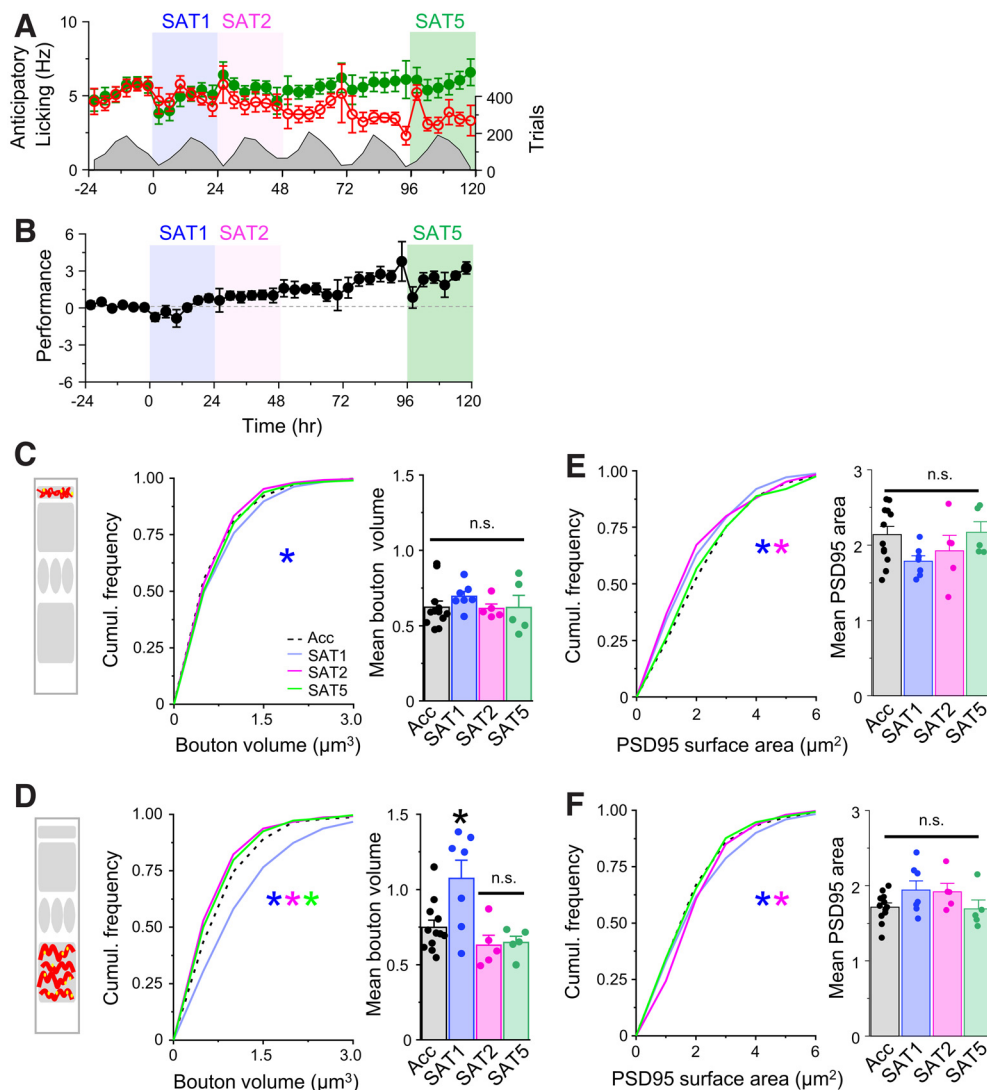


Figure 10. Morphologic changes at thalamocortical synapses are transient during learning. **A**, Anticipatory licking frequency of mice to stimulus (green closed circles) and blank (red open circles) trials across 1 d of acclimation and multiple days of SAT. The average number of trials across time bins shown in gray. **B**, Performance ($L_{stim} - L_{blank}$) across 5 d of SAT. **C**, Left, Schematic of L1 POM synapses from selected axonal segments. Middle, Cumulative distribution histogram of POM boutons in L1 from acclimation control (Acc; dashed black line; 960 boutons; 12 mice), SAT1 (blue line; 560 boutons; 7 mice), SAT2 (pink line; 400 boutons; 5 mice), and SAT5 (green line; 400 boutons; 5 mice) animals. K-S tests, Acc versus SAT1 ($p = 0.012$), Acc versus SAT2 ($p = 0.26$), and Acc versus SAT5 ($p = 0.34$). Right, Animal-averaged mean bouton volume + SEM by animal (solid dots); $N = 12$ Acc, 7 SAT1, 5 SAT2, 5 SAT5 mice; $F_{(3,25)} = 0.95$; $p = 0.43$. **D**, Left, Schematic of L5a POM synapses from selected axonal segments. Middle, Cumulative distribution histogram of POM boutons in L5 from Acc (dashed black line; 960 boutons; 12 mice), SAT1 (blue line; 560 boutons; 7 mice), SAT2 (pink line; 400 boutons; 5 mice), and SAT5 (green line; 400 boutons; 5 mice) animals. K-S tests, Acc versus SAT1 ($p = 4.53 \times 10^{-5}$), and Acc versus SAT5 ($p = 0.021$). Right, Animal-averaged mean bouton volume + SEM by animal (solid dots); $N = 12$ Acc, 7 SAT1, 5 SAT2, 5 SAT5 mice; $F_{(3,25)} = 6.54$; $p = 0.0021$. Tukey's p (Acc vs SAT1) = 0.013; Tukey's p (Acc vs SAT2) = 0.70; Tukey's p (Acc vs SAT5) = 0.79. **E**, Left, Cumulative distribution histogram of POM-assigned synapses in L1 showing an increase in synaptic size after training from Acc (dashed black line; 300 puncta; 12 mice) and SAT1 (blue line; 175 puncta; 7 mice), SAT2 (pink line; 125 puncta; 5 mice), and SAT5 (green line; 125 puncta; 5 mice) animals. K-S tests, Acc versus SAT1 ($p = 0.042$), Acc versus SAT2 ($p = 0.021$), and Acc versus SAT5 ($p = 0.75$). Right, Animal-averaged mean bouton volume + SEM by animal (solid dots); $N = 12$ Acc, 7 SAT1, 5 SAT2, 5 SAT5 mice; $F_{(3,25)} = 1.99$; $p = 0.14$. **F**, Left, Cumulative distribution histogram of POM-assigned synapses in L5a showing renormalization of synaptic size after 5 d SAT. Acc (dashed black line; 720 puncta; 12 mice), SAT1 (blue line; 420 puncta; 7 mice), SAT2 (pink line; 300 puncta; 5 mice), and SAT5 (green line; 300 puncta; 5 mice) animals. K-S tests, Acc versus SAT1 ($p = 0.024$), Acc versus SAT2 ($p = 0.0031$), and Acc versus SAT5 ($p = 0.84$). Right, Averaged mean puncta surface area + SEM by animal (solid dots); $N = 12$ Acc, 7 SAT1, 5 SAT2, 5 SAT5 mice; $F_{(3,25)} = 1.91$; $p = 0.15$. Data from Acc and SAT1 animals replotted from earlier figures. Groups were compared using one-way ANOVA followed by *post hoc* Tukey tests for assessing significance for bar graphs in **C–F**.

However, identifying coordinated input- and target-specific changes has been elusive, making it difficult to determine how network function can be altered by experience and learning. Although EM images can provide high-resolution data for synapse detection, tools for pathway-specific labeling have only recently become available (Tabata et al., 2019; Rae et al., 2021), and their application is not easily adapted to the analysis of large numbers of brain areas and animal subjects, critical for learning studies. Here, we use high-throughput, fluorescence-based methods for

input- and target-specific synapse identification to examine anatomic changes at thalamocortical synapses occurring during sensory learning. We find that training in a sensory association task rapidly drives layer-specific changes in both presynaptic and postsynaptic compartments at POM thalamocortical inputs onto L5 Pyr neurons. Surprisingly, increases in size of both axonal boutons and postsynaptic structures were concentrated within L5a, and the small increase in axonal bouton size in L1 was not accompanied by corresponding postsynaptic changes. The close corroboration of

anatomic data with electrophysiological recordings indicates that fluorescence-based measurements of synaptic connectivity and plasticity are feasible and can provide a platform for discovery in other systems.

Rapid changes in presynaptic and postsynaptic structures during SAT

A great deal of electrophysiological and biochemical evidence indicates that long-term potentiation at the majority of glutamatergic synapses can be attributed to postsynaptic AMPAR addition (Diering and Hugarir, 2018). However, presynaptic changes have also been observed, particularly from *in vitro* studies during electrical (Bourne et al., 2013; Bell et al., 2014) or chemically evoked synaptic potentiation (Meyer et al., 2014; Hruska et al., 2018; Sun et al., 2021; Wegner et al., 2022). Coordinated input- and target-specific anatomic changes have not been well studied *in vivo*. Although structural properties of presynaptic and postsynaptic components are tightly correlated under basal conditions (Harris and Stevens, 1989) and are predictive of synaptic strength (Cheetham et al., 2014), whether and when morphologic changes in axonal boutons accompany postsynaptic modifications during behaviorally relevant plasticity remains unclear.

Our data indicate that both presynaptic and postsynaptic structures can be coordinately modified at thalamocortical synapses during the early stages of sensory learning at a time when these synapses are functionally enhanced. Increases in POM bouton size at the onset of SAT were most pronounced in L5a and were less obvious in L1, a site of well-documented synaptic changes in other experimental paradigms, particularly during motor learning (Fortin et al., 2014; Chen et al., 2015; Hasegawa et al., 2020). Thalamocortical bouton changes were transient, resolving to baseline values after 2 d of training. POM-associated PSD95 puncta within L5 also showed a significant, albeit smaller, increase in size after 1 d of SAT and were slower to return to baseline.

Although POM boutons increased in size, presynaptic release properties of these synapses were not apparently altered by SAT (Audette et al., 2019), although the use of channelrhodopsin to isolate POM afferent activity may complicate the interpretation of these results. The marked increase in bouton size in this behavioral paradigm will facilitate future studies to identify the trigger for presynaptic modification and also determine the functional consequences of this enlargement.

Anatomical evidence for synaptic potentiation in L1

In vivo imaging studies have shown that axonal boutons and dendritic spines in the neocortex are modified during sensory and motor learning. Prior studies have either focused on axons or dendritic spines, particularly on Pyr neurons that have an apical dendrite in L1 that is amenable to *in vivo* imaging studies (Trachtenberg et al., 2002; Yang et al., 2009; Kuhlman et al., 2014; Chen et al., 2015; Hasegawa et al., 2020; Pardi et al., 2020; Graves et al., 2021). Thus, the specific pathways that are altered during sensory and motor learning and their attached presynaptic and postsynaptic partners have not been well defined.

Despite well-documented structural plasticity of presynaptic and postsynaptic elements in L1, we only found a modest presynaptic increase without a corresponding change in postsynaptic sizes in POM thalamocortical synaptic morphology in this layer. Instead, our fluorescence-based analysis indicated that POM-assigned PSD95 synapses at the apical dendrites of L5 Pyr became significantly smaller in L1 at the early stages of SAT. This cannot be easily explained by

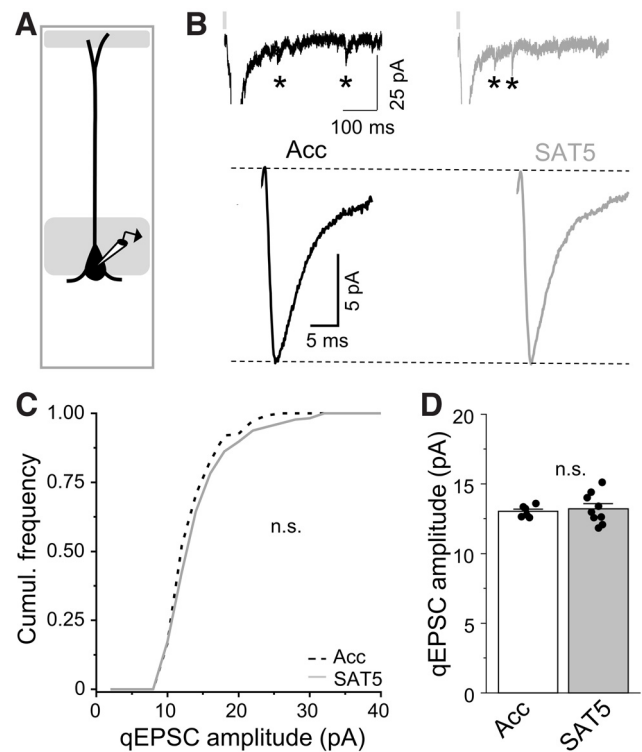


Figure 11. Extended training renormalizes thalamocortical synapse strength. **A**, Schematic showing whole-cell recording from a L5 Pyr in an acute brain slice from barrel cortex, with ChR2-expressing POM axons in gray. **B**, Top, Example traces for P0m-evoked responses in Sr^{2+} -containing ACSF from L5 Pyr neurons from acclimation control (Acc; black) and SAT5 (gray) trained mice. Asterisks indicate individual isolated quantal events. Bottom, Global average qEPSCs from all cells from Acc and SAT5 animals. **C**, Cumulative distributions of individual qEPSC amplitudes from Acc (black dashed line; 175 events total from 7 cells) and SAT5 (gray line; 225 events total from 9 cells). K–S tests, $p = 0.14$. **D**, Mean qEPSC amplitudes \pm SEM by animal (solid dots); $N = 7$ cells from four Acc and 9 cells from six SAT5 mice. Unpaired $t_{(17)} = 0.68$; $p = 0.51$.

limitations of this approach, since the same methods demonstrated increases in POM-assigned PSD95 size within L5a.

Previously characterized increases in thalamocortical synaptic strength are likely to reflect changes within L5 itself because of space-clamp constraints in synaptic recordings (Audette et al., 2019). However, as the Rbp4-Cre transgenic line used for these studies labels both intertelencephalic and pyramidal tract Pyr neurons, it is possible that a subset of synapses onto one of the targets might be selectively weakened or that there are balanced alterations on these two cell types that obscure a detectable effect.

Training-dependent reductions in spine density at apical dendrites of L5 Pyr in somatosensory cortex have been observed in eyeblink conditioning (Joachimsthaler et al., 2015), a learning paradigm that may have some overlap with the SAT deployed here. Our data suggest that synaptic plasticity at proximal and distal synapses may be differentially regulated even for the same presynaptic input, an important observation given specialized properties of the apical dendrite in Pyr neurons (Takahashi et al., 2016; Lafourcade et al., 2022). Indeed, electrophysiological studies indicate that spike-timing-dependent plasticity may be more effective in proximal dendrites, and the delayed timing of dendritic Ca^{2+} events in tufts might drive synaptic depression (Letzkus et al., 2006; Sjöström and Häusser, 2006).

Importantly, our data do not rule out potential strengthening of excitatory synapses from other inputs on L5 Pyr tufts (e.g.,

perirhinal inputs; Doron et al., 2020). Indeed, the increase in bouton size in L1 contrasts with the reduction of postsynaptic size and suggests that higher-order thalamic inputs on other target cells, such as L2/3 Pyr or L1 interneurons (Audette et al., 2018; Pardi et al., 2020), may be selectively modified. In addition, many other studies examining synaptic dynamics in L1 during learning have focused on motor cortex, which may be critically different from sensory cortex.

Transient changes in synaptic morphology

Neocortical circuits are modified by experience and during learning, and synaptic changes may occur before changes in behavior (Jurjut et al., 2017; Audette et al., 2019). Interestingly, multiple studies suggest that changes in sensory and motor cortex may not be long lasting, even when task performance remains high (Yotsumoto et al., 2008; Reed et al., 2011; Elias et al., 2015; Pruitt et al., 2016).

Our data show that morphologic changes at thalamocortical synapses are rapidly initiated at the onset of training and then renormalize as animals acquire the stimulus–outcome association, providing a structural correlate for functional data obtained in prior studies. Although acquisition of this sensory association measured by anticipatory licking is heterogeneous across animals and can take several days to emerge (Lee et al., 2021), we did not observe a correlation between larger synaptic changes and behavioral learning. This may be because of the inherent heterogeneity conferred by viral labeling approaches or because these changes are highly dynamic during the early training period (Barth and Ray, 2019). It remains an open question what processes trigger synaptic renormalization during learning; these might be intrinsic, homeostatic properties of synapses or may be related to changes in neuromodulatory dynamics or motor output as behavioral responses are modified over time. High-throughput anatomic techniques that can be deployed across large numbers of animals are well suited to manipulate defined variables to test these hypotheses.

Advantages of fluorescence-based synaptic analysis

Fluorescence-based labeling of presynaptic and postsynaptic structures takes advantage of genetically encoded tags and a rainbow of fluorophores for input- and target specific analysis. Fluorescence-based methods can increase the number of synapses analyzed by 10–100 times compared with EM, which is typically carried on single subjects. Also, it is more amenable to replication in larger groups of subjects, which is important for learning studies where there can be great variability in the speed of learning. The use of fluorescence-based methods for synapse detection has been widespread, although typically at small scale (Di Cristo et al., 2004; Mishchenko, 2010; Donato et al., 2013; Takesian et al., 2018), despite the fact that the distance between presynaptic and postsynaptic elements is below the diffraction limit and is probabilistic, not definitive. Although correlated light EM could in theory resolve this, it comes at a significant cost in terms of speed in sample preparation and image acquisition, as well as the availability of EM instrumentation, and is not widely accessible.

Advances in digital analysis can facilitate insights from cell-type and input-specific synapse labeling as parameters can be rapidly adjusted to test the validity of experimental results. We used the ease of digital synapse detection to compare synapse properties when distance parameters for synapse assignment were increased to exclude direct contacts. This analysis showed that only PSD95 puncta touching POM axonal boutons showed a

significant shift in size with SAT versus puncta that were only 0.5–1 μm more distant. Putative synaptic contacts detected using digital analysis will necessarily contain false positives, and it is likely that the effect sizes for thalamocortical plasticity are larger than described here. Despite uncertainty in location of fluorescence-based images from confocal microscopy, our results are well corroborated by electrophysiological measurements at the same synapses.

Because neither presynaptic nor postsynaptic structures were labeled to saturation, we were unable to compare the density of synapses across animals and conditions. Longitudinal *in vivo* imaging would address this, albeit at a cost of resolution. Although immunohistochemical labeling of synaptic markers could provide a more comprehensive view of synaptic changes, identification of antibodies that work well in tissue and challenges in sample preparation have slowed progress (Micheva and Smith, 2007; Kim et al., 2022). In addition, molecules used as bona fide synaptic markers may not be uniformly expressed within a class of synapses (Graziano et al., 2008), and uneven antibody penetration into tissue sections also poses further limitations.

An advantage of sparse labeling provided by viral transduction is an improved ability to detect and isolate presynaptic and postsynaptic signals, facilitating analysis compared with approaches where synapses are densely labeled and overlapping (Fortin et al., 2014; Graves et al., 2021; Dempsey et al., 2022). Although care must be taken to identify the correct parameters for comparison (i.e., properties of detected contacts, not their overall density in tissue), our data demonstrate that significant biological insights can be obtained from these approaches.

References

- Audette NJ, Urban-Ciecko J, Matsushita M, Barth AL (2018) POM thalamocortical input drives layer-specific microcircuits in somatosensory cortex. *Cereb Cortex* 28:1312–1328.
- Audette NJ, Bernhard SM, Ray A, Stewart LT, Barth AL (2019) Rapid plasticity of higher-order thalamocortical inputs during sensory learning. *Neuron* 103:277–291.e4.
- Barth AL, Ray A (2019) Progressive circuit changes during learning and disease. *Neuron* 104:37–46.
- Bell ME, Bourne JN, Chirillo MA, Mendenhall JM, Kuwajima M, Harris KM (2014) Dynamics of nascent and active zone ultrastructure as synapses enlarge during long-term potentiation in mature hippocampus. *J Comp Neurol* 522:3861–3884.
- Bensussen S, Shankar S, Ching KH, Zemel D, Ta TL, Mount RA, Shroff SN, Gritton HJ, Fabris P, Vanbenschoten H, Beck C, Man H-Y, Han X (2020) A viral toolbox of genetically encoded fluorescent synaptic tags. *iScience* 23:101330.
- Bernhard SM, Lee J, Zhu M, Hsu A, Erskine A, Hires SA, Barth AL (2020) An automated homebase system for multiwhisker detection and discrimination learning in mice. *PLoS One* 15:e0232916.
- Biane JS, Takashima Y, Scanziani M, Conner JM, Tuszynski MH (2016) Thalamocortical projections onto behaviorally relevant neurons exhibit plasticity during adult motor learning. *Neuron* 89:1173–1179.
- Bock DD, Lee W-CA, Kerlin AM, Andermann ML, Hood G, Wetzel AW, Yurgenson S, Soucy ER, Kim HS, Reid RC (2011) Network anatomy and *in vivo* physiology of visual cortical neurons. *Nature* 471:177–182.
- Bopp R, Holler-Rickauer S, Martin KAC, Schuhknecht GFP (2017) An ultrastructural study of the thalamic input to layer 4 of primary motor and primary somatosensory cortex in the mouse. *J Neurosci* 37:2435–2448.
- Bourne JN, Chirillo MA, Harris KM (2013) Presynaptic ultrastructural plasticity along CA3→CA1 axons during long-term potentiation in mature hippocampus. *J Comp Neurol* 521:3898–3912.
- Cane M, Maco B, Knott G, Holtmaat A (2014) The relationship between PSD-95 clustering and spine stability *in vivo*. *J Neurosci* 34:2075–2086.

- Chandrasekaran S, Navlakha S, Audette NJ, McCreary DD, Suhan J, Bar-Joseph Z, Barth AL (2015) Unbiased, high-throughput electron microscopy analysis of experience-dependent synaptic changes in the neocortex. *J Neurosci* 35:16450–16462.
- Cheetham CEJ, Barnes SJ, Albieri G, Knott GW, Finnerty GT (2014) Pansynaptic enlargement at adult cortical connections strengthened by experience. *Cereb Cortex* 24:521–531.
- Chen SX, Kim AN, Peters AJ, Komiyama T (2015) Subtype-specific plasticity of inhibitory circuits in motor cortex during motor learning. *Nat Neurosci* 18:1109–1115.
- Dempsey WP, Du Z, Nadtchuy A, Smith CD, Czajkowski K, Andreev A, Robson DN, Li JM, Applebaum S, Truong TV, Kesselman C, Fraser SE, Arnold DB (2022) Regional synapse gain and loss accompany memory formation in larval zebrafish. *Proc Natl Acad Sci U S A* 119:e2107661119.
- Di Cristo G, Wu C, Chattopadhyaya B, Ango F, Knott G, Welker E, Svoboda K, Huang ZJ (2004) Subcellular domain-restricted GABAergic innervation in primary visual cortex in the absence of sensory and thalamic inputs. *Nat Neurosci* 7:1184–1186.
- Diering GH, Hugarir RL (2018) The AMPA receptor code of synaptic plasticity. *Neuron* 100:314–329.
- Donato F, Rompani SB, Caroni P (2013) Parvalbumin-expressing basket-cell network plasticity induced by experience regulates adult learning. *Nature* 504:272–276.
- Doron G, Shin JN, Takahashi N, Drüke M, Bocklisch C, Skenderi S, de Mont L, Toumazou M, Ledderose J, Brecht M, Naud R, Larkum ME (2020) Perirhinal input to neocortical layer 1 controls learning. *Science* 370:eaz3136.
- Dresbach T, Qualmann B, Kessels MM, Garner CC, Gundelfinger ED (2001) The presynaptic cytomatrix of brain synapses. *Cell Mol Life Sci* 58:94–116.
- Ehrlich I, Malinow R (2004) Postsynaptic density 95 controls AMPA receptor incorporation during long-term potentiation and experience-driven synaptic plasticity. *J Neurosci* 24:916–927.
- Elias GA, Bieszczad KM, Weinberger NM (2015) Learning strategy refinement reverses early sensory cortical map expansion but not behavior: support for a theory of directed cortical substrates of learning and memory. *Neurobiol Learn Mem* 126:39–55.
- Fortin DA, Tillo SE, Yang G, Rah J-C, Melander JB, Bai S, Soler-Cedeño O, Qin M, Zemelman BV, Guo C, Mao T, Zhong H (2014) Live imaging of endogenous PSD-95 using ENABLED: a conditional strategy to fluorescently label endogenous proteins. *J Neurosci* 34:16698–16712.
- Fu M, Yu X, Lu J, Zuo Y (2012) Repetitive motor learning induces coordinated formation of clustered dendritic spines *in vivo*. *Nature* 483:92–95.
- Gerfen CR, Paletzki R, Heintz N (2013) GENSAT BAC Cre-recombinase driver lines to study the functional organization of cerebral cortical and basal ganglia circuits. *Neuron* 80:1368–1383.
- Gilad A, Helmchen F (2020) Spatiotemporal refinement of signal flow through association cortex during learning. *Nat Commun* 11:1744.
- Graves AR, Roth RH, Tan HL, Zhu Q, Bygrave AM, Lopez-Ortega E, Hong I, Spiegel AC, Johnson RC, Vogelstein JT, Tward DJ, Miller MI, Hugarir RL (2021) Visualizing synaptic plasticity *in vivo* by large-scale imaging of endogenous AMPA receptors. *Elife* 10:e66809.
- Gray NW, Weimer RM, Bureau I, Svoboda K (2006) Rapid redistribution of synaptic PSD-95 in the neocortex *in vivo*. *PLoS Biol* 4:e370.
- Graziano A, Liu X-B, Murray KD, Jones EG (2008) Vesicular glutamate transporters define two sets of glutamatergic afferents to the somatosensory thalamus and two thalamocortical projections in the mouse. *J Comp Neurol* 507:1258–1276.
- Gross GG, Junge JA, Mora RJ, Kwon H-B, Olson CA, Takahashi TT, Liman ER, Ellis-Davies GCR, McGee AW, Sabatini BL, Roberts RW, Arnold DB (2013) Recombinant probes for visualizing endogenous synaptic proteins in living neurons. *Neuron* 78:971–985.
- Harris KM, Stevens JK (1989) Dendritic spines of CA 1 pyramidal cells in the rat hippocampus: serial electron microscopy with reference to their biophysical characteristics. *J Neurosci* 9:2982–2997.
- Hasegawa R, Ebina T, Tanaka YR, Kobayashi K, Matsuzaki M (2020) Structural dynamics and stability of corticocortical and thalamocortical axon terminals during motor learning. *PLoS One* 15:e0234930.
- Heise C, Schroeder JC, Schoen M, Halbedl S, Reim D, Woelfle S, Kreutz MR, Schmeisser MJ, Boeckers TM (2016) Selective localization of shanks to VGLUT1-positive excitatory synapses in the mouse hippocampus. *Front Cell Neurosci* 10:106.
- Hruska M, Henderson N, Le Marchand SJ, Jafri H, Dalva MB (2018) Synaptic nanomodules underlie the organization and plasticity of spine synapses. *Nat Neurosci* 21:671–682.
- Joachimsthaler B, Brugger D, Skodras A, Schwarz C (2015) Spine loss in primary somatosensory cortex during trace eyeblink conditioning. *J Neurosci* 35:3772–3781.
- Jurjut O, Georgieva P, Busse L, Katzner S (2017) Learning enhances sensory processing in mouse V1 before improving behavior. *J Neurosci* 37:6460–6474.
- Kasthuri N, et al. (2015) Saturated reconstruction of a volume of neocortex. *Cell* 162:648–661.
- Kim N, Bahn S, Choi JH, Kim JS, Rah J-C (2022) Synapses from the motor cortex and a high-order thalamic nucleus are spatially clustered in proximity to each other in the distal tuft dendrites of mouse somatosensory cortex. *Cereb Cortex* 32:737–754.
- Kuhlman SJ, O'Connor DH, Fox K, Svoboda K (2014) Structural plasticity within the barrel cortex during initial phases of whisker-dependent learning. *J Neurosci* 34:6078–6083.
- Kuljis DA, Park E, Telmer CA, Lee J, Ackerman DS, Bruchez MP, Barth AL (2019) Fluorescence-based quantitative synapse analysis for cell type-specific connectomics. *eNeuro* 6:ENEURO.0193-19.2019.
- Kuljis DA, Micheva KD, Ray A, Wegner W, Bowman R, Madison DV, Willig KI, Barth AL (2021) Gephyrin-lacking PV synapses on neocortical pyramidal neurons. *Int J Mol Sci* 22:10032.
- Lacefield CO, Pnevmatikakis EA, Paninski L, Bruno RM (2019) Reinforcement learning recruits somata and apical dendrites across layers of primary sensory cortex. *Cell Rep* 26:2000–2008.e2.
- Lafourcade M, van der Goes M-SH, Vardalaki D, Brown NJ, Voigts J, Yun DH, Kim ME, Ku T, Harnett MT (2022) Differential dendritic integration of long-range inputs in association cortex via subcellular changes in synaptic AMPA-to-NMDA receptor ratio. *Neuron* 110:1532–1546.e4.
- Lai CSW, Adler A, Gan W-B (2018) Fear extinction reverses dendritic spine formation induced by fear conditioning in the mouse auditory cortex. *Proc Natl Acad Sci U S A* 115:9306–9311.
- Lee J, Urban-Ciecko J, Park E, Zhu M, Myal SE, Margolis DJ, Barth AL (2021) FosGFP expression does not capture a sensory learning-related engrain in superficial layers of mouse barrel cortex. *Proc Natl Acad Sci U S A* 118:e2112212118.
- Letzkus JJ, Kampa BM, Stuart GJ (2006) Learning rules for spike timing-dependent plasticity depend on dendritic synapse location. *J Neurosci* 26:10420–10429.
- Lucantonio F, Kim E, Su Z, Chang AJ, Bari BA, Cohen JY (2021) Aversive stimuli bias corticothalamic responses to motivationally significant cues. *Elife* 10:e57634.
- Meyer D, Bonhoeffer T, Scheuss V (2014) Balance and stability of synaptic structures during synaptic plasticity. *Neuron* 82:430–443.
- Micheva KD, Smith SJ (2007) Array tomography: a new tool for imaging the molecular architecture and ultrastructure of neural circuits. *Neuron* 55:25–36.
- Micheva KD, Busse B, Weiler NC, O'Rourke N, Smith SJ (2010) Single-synapse analysis of a diverse synapse population: proteomic imaging methods and markers. *Neuron* 68:639–653.
- Mishchenko Y (2010) On optical detection of densely labeled synapses in neuropil and mapping connectivity with combinatorially multiplexed fluorescent synaptic markers. *PLoS One* 5:e8853.
- Moreno Manrique JF, Voit PR, Windsor KE, Karla AR, Rodriguez SR, Beaudoin GMJ (2021) SynapseJ: an automated, synapse identification macro for ImageJ. *Front Neural Circuits* 15:731333.
- Pardi MB, Vogenstahl J, Dalmay T, Spanò T, Pu D-L, Naumann LB, Kretschmer F, Sprekeler H, Letzkus JJ (2020) A thalamocortical top-down circuit for associative memory. *Science* 370:844–848.
- Pruitt DT, Schmid AN, Danaphongse TT, Flanagan KE, Morrison RA, Kilgard MP, Rennaker RL, Hays SA (2016) Forelimb training drives transient map reorganization in ipsilateral motor cortex. *Behav Brain Res* 313:10–16.
- Rae J, Ferguson C, Ariotti N, Webb RI, Cheng H-H, Mead JL, Riches JD, Hunter DJ, Martel N, Baltos J, Christopoulos A, Bryce NS, Cagigas ML, Fonseca S, Sayre ME, Hardeman EC, Gunning PW, Gambin Y, Hall TE, Parton RG (2021) A robust method for particulate detection of a genetic tag for 3D electron microscopy. *Elife* 10:e64630.

- Reed A, Riley J, Carraway R, Carrasco A, Perez C, Jakkamsetti V, Kilgard MP (2011) Cortical map plasticity improves learning but is not necessary for improved performance. *Neuron* 70:121–131.
- Riout-Pedotti MS, Friedman D, Donoghue JP (2000) Learning-induced LTP in neocortex. *Science* 290:533–536.
- Rodriguez-Moreno J, Rollenhagen A, Arlandis J, Santuy A, Merchan-Pérez A, DeFelipe J, Lübke JHR, Clasca F (2018) Quantitative 3D ultrastructure of thalamocortical synapses from the “lemniscal” ventral posteromedial nucleus in mouse barrel cortex. *Cereb Cortex* 28:3159–3175.
- Rodriguez-Moreno J, Porrero C, Rollenhagen A, Rubio-Teves M, Casas-Torremocha D, Alonso-Nanclares L, Yakoubi R, Santuy A, Merchan-Pérez A, DeFelipe J, Lübke JHR, Clasca F (2020) Area-specific synapse structure in branched posterior nucleus axons reveals a new level of complexity in thalamocortical networks. *J Neurosci* 40:2663–2679.
- Schoonover CE, Tapia J-C, Schilling VC, Wimmer V, Blazeski R, Zhang W, Mason CA, Bruno RM (2014) Comparative strength and dendritic organization of thalamocortical and corticocortical synapses onto excitatory layer 4 neurons. *J Neurosci* 34:6746–6758.
- Schuman B, Dellal S, Prönneke A, Machold R, Rudy B (2021) Neocortical layer 1: an elegant solution to top-down and bottom-up integration. *Annu Rev Neurosci* 44:221–252.
- Sheng M, Hoogenraad CC (2007) The postsynaptic architecture of excitatory synapses: a more quantitative view. *Annu Rev Biochem* 76:823–847.
- Sjöström PJ, Häusser M (2006) A cooperative switch determines the sign of synaptic plasticity in distal dendrites of neocortical pyramidal neurons. *Neuron* 51:227–238.
- Subramanian J, Michel K, Benoit M, Nedivi E (2019) CPG15/neuritin mimics experience in selecting excitatory synapses for stabilization by facilitating PSD95 recruitment. *Cell Rep* 28:1584–1595.e5.
- Sun Y, Smirnov M, Kamasawa N, Yasuda R (2021) Rapid ultrastructural changes in the PSD and surrounding membrane after induction of structural LTP in single dendritic spines. *J Neurosci* 41:7003–7014.
- Tabata S, Jevtic M, Kurashige N, Fuchida H, Kido M, Tani K, Zenmyo N, Uchinomiya S, Harada H, Itakura M, Hamachi I, Shigemoto R, Ojida A (2019) Electron microscopic detection of single membrane proteins by a specific chemical labeling. *iScience* 22:256–268.
- Takahashi N, Oertner TG, Hegemann P, Larkum ME (2016) Active cortical dendrites modulate perception. *Science* 354:1587–1590.
- Takesian AE, Bogart LJ, Lichtman JW, Hensch TK (2018) Inhibitory circuit gating of auditory critical-period plasticity. *Nat Neurosci* 21:218–227.
- Tennant KA, Taylor SL, White ER, Brown CE (2017) Optogenetic rewiring of thalamocortical circuits to restore function in the stroke injured brain. *Nat Commun* 8:15879.
- Trachtenberg JT, Chen BE, Knott GW, Feng G, Sanes JR, Welker E, Svoboda K (2002) Long-term in vivo imaging of experience-dependent synaptic plasticity in adult cortex. *Nature* 420:788–794.
- Wegner W, Steffens H, Gregor C, Wolf F, Willig KI (2022) Environmental enrichment enhances patterning and remodeling of synaptic nanoarchitecture as revealed by STED nanoscopy. *Elife* 11:e73603.
- Wimmer VC, Bruno RM, de Kock CPJ, Kuner T, Sakmann B (2010) Dimensions of a projection column and architecture of VPM and POM axons in rat vibrissa cortex. *Cereb Cortex* 20:2265–2276.
- Yang G, Pan F, Gan W-B (2009) Stably maintained dendritic spines are associated with lifelong memories. *Nature* 462:920–924.
- Yotsumoto Y, Watanabe T, Sasaki Y (2008) Different dynamics of performance and brain activation in the time course of perceptual learning. *Neuron* 57:827–833.
- Zhang G-W, Shen L, Zhong W, Xiong Y, Zhang LI, Tao HW (2018) Transforming sensory cues into aversive emotion via septal-habenular pathway. *Neuron* 99:1016–1028.e5.